Printing-based assembly of quadruple-junction four-terminal microscale solar cells and their use in high-efficiency modules

Xing Sheng[1†], Christopher A. Bower[2†], Salvatore Bonafede[2], John W. Wilson[2], Brent Fisher[2], Matthew Meitl[2], Homan Yuen[3], Shuodao Wang[1], Ling Shen[4], Anthony R. Banks[5], Christopher J. Corcoran[6], Ralph G. Nuzzo[1,6], Scott Burroughs[2]* and John A. Rogers[1,6]*

Expenses associated with shipping, installation, land, regulatory compliance and on-going maintenance and operations of utility-scale photovoltaics can be significantly reduced by increasing the power conversion efficiency of solar modules[1] through improved materials, device designs and strategies for light management[2–4]. Single-junction cells have performance constraints defined by their Shockley–Queisser limits[5]. Multi-junction cells[6–12] can achieve higher efficiencies, but epitaxial and current matching requirements between the single junctions in the devices hinder progress. Mechanical stacking of independent multi-junction cells[13–19] circumvents these disadvantages. Here we present a fabrication approach for the realization of mechanically assembled multi-junction cells using materials and techniques compatible with large-scale manufacturing. The strategy involves printing-based stacking of microscale solar cells, sol–gel processes for interlayers with advanced optical, electrical and thermal properties, together with unusual packaging techniques, electrical matching networks, and compact ultrahigh-concentration optics. We demonstrate quadruple-junction, four-terminal solar cells with measured efficiencies of 43.9% at concentrations exceeding 1,000 suns, and modules with efficiencies of 36.5%.

The photovoltaic module efficiency impacts almost every component of the aggregate system cost, from materials to manufacturing, to installation and operations[1]. Single-junction (SJ) solar cells are already near theoretical efficiency limits defined by thermalization losses and sub-bandgap transparency[2–5]. Parallel use of multiple, separated SJ cells with spectral-splitting optical elements[20–22] can be attractive, but the complexity in manufacturing, alignment and light management hinder prospects for practical use. Devices that incorporate multiple junctions (that is, sub-cells) in monolithic stacks, known as multi-junction (MJ) cells[6–19], provide an attractive route to ultrahigh efficiency. Over the past decade, increases in the absolute efficiency of MJ cells correspond to nearly 1% per year, reaching values that are at present ~44%[6–12]. Further improvements, however, will require solutions to daunting challenges in achieving lattice-matched[7,8] or metamorphic[8–12] epitaxial growth in complex stacks and in maintaining current-matched outputs from each of the sub-cells. Mechanical stacking of separately grown SJ or MJ materials represents a well-explored alternative route to MJ devices[13–19] that have recently demonstrated very high efficiencies[15]. This process involves physical wafer bonding, followed by eliminating the top and/or bottom wafers. One option for bonding uses direct, high-temperature wafer fusion techniques[13–15]. The electrically conducting interface that results, however, retains the requirement of current matching. This demand becomes challenging to maintain as the number of sub-cells in the MJ device increases, owing to natural variations in the terrestrial solar spectrum. An alternative approach uses thick, insulating organic adhesives, with double-sided, multilayer antireflective coatings and multi-terminal connections[16–19]. Here, the resulting MJ cells suffer from interface reflections, poor heat flow characteristics and often unfavorable thermo-mechanical interface stresses at high irradiance concentration. Despite research and development during the past ~25 years, neither of these bonding strategies at present offers a realistic means for manufacturing or for viable multiple stacking operations.

This paper describes concepts to bypass many of the limitations of these and other previously explored technologies. Here, printing-based methods enable high-throughput physical assembly of arrays of stacked, microscale MJ solar cells using high-performance, released thin-film materials via epitaxial liftoff processes. An infrared transparent and refractive-index-matched layer of a chalcogenide glass (arsenic triselenide, As_2Se_3) serves as a thermally conductive and electrically insulating interface layer in these stacks. Advanced packaging techniques, electrical matching networks and dual-stage imaging lenses yield modules with efficiencies of 36.5%.

Figure 1a schematically illustrates the structure and assembly process for a quadruple-junction, four-terminal microscale solar cell, with an active area of $600 \times 600 \, \mu m^2$ (see Methods and Supplementary Figs 1–10 for fabrication details). The top cell uses a three-junction (3J) design based on InGaP/GaAs/InGaAsNSb (bandgaps of 1.9 eV/1.4 eV/1.0 eV) (ref. 7), grown lattice matched on a GaAs substrate and released by eliminating a sacrificial layer of AlInP at the base of the stack[23,24]. A tri-layer anti-reflective coating (ARC) ensures efficient transmission of light into this 3J cell. The bottom cell (lateral dimensions matched to the top cell) is a diffused-junction Ge device[25]. Figure 1b,c provides
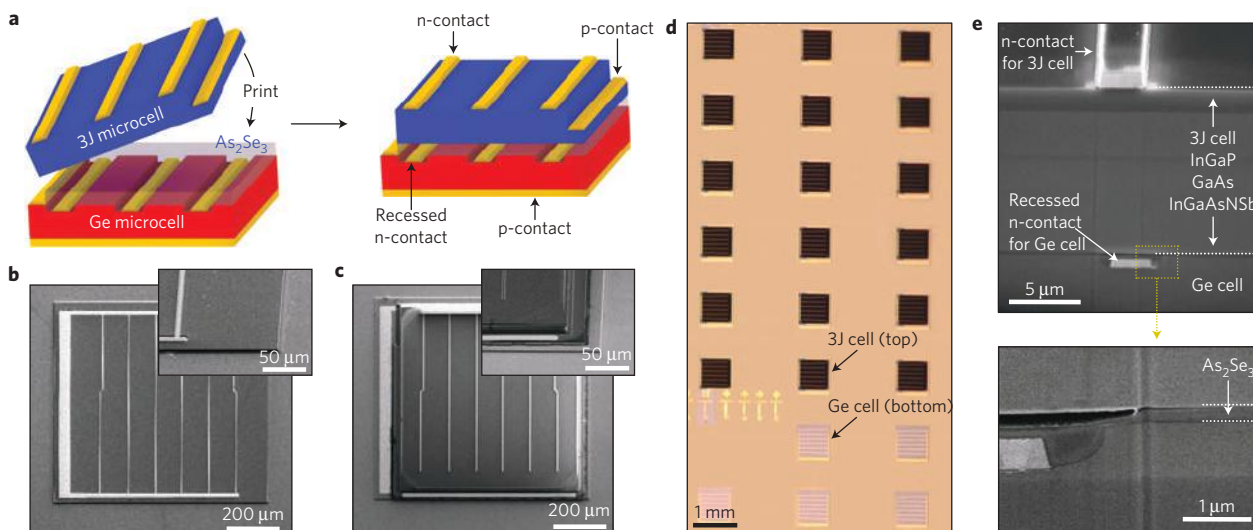
Figure 1 | Schematic illustrations and images of quadruple-junction four-terminal microscale solar cells assembled using a printing-based method and an As$_2$Se$_3$ interface material. a, Schematic illustration of a cell from a 3J thin-film stack of InGaP/GaAs/InGaAsNSb derived from epitaxial growth and liftoff and a separate 1J Ge cell, before (left) and after (right) assembly by transfer printing. The As$_2$Se$_3$ layer (light blue) and the recessed metal contact lines on the top of the Ge cell ensure excellent optical, electrical and thermal properties at the interface. **b,c**, SEM images (top and magnified tilted views) of a Ge cell before (**b**) and after (**c**) printing a 3J cell on top. **d**, Optical micrograph of an array of 3J/Ge microscale solar cells. The bottom part of this image shows alignment features for the printing process, and several bare Ge cells. **e**, SEM image (cross-sectional view) of a 3J/Ge cell, showing the aligned metal contact lines and the As$_2$Se$_3$ layer. Inset: High-magnification image of the interface region.

scanning electron microscope (SEM) images of a typical Ge cell before and after delivery of a 3J cell onto its surface, respectively, by transfer printing[26]. This assembly process occurs in a high-throughput, parallel fashion, to allow simultaneous formation of arrays of stacked MJ cells, in a fully automated step-and-repeat mode with high yields (>95%) and accurate overlay registration (<2 μm), as illustrated by the optical microscope image in Fig. 1d. The Ge cells use recessed grid metallization on the top surface to enable high-quality contact and bonding at the interface. A layer of As$_2$Se$_3$ (~300 nm thick) spin-cast on top of the Ge cell using a sol–gel process[27] provides a low-loss optical interface, with minimal thermal resistance and excellent electrical isolation, as described in detail subsequently. The cross-sectional SEM images in Fig. 1e illustrate the aligned and recessed metal contacts as well as the As$_2$Se$_3$ interface layer. In such a stacked 3J/Ge structure, the top 3J cell captures light from 300 nm to 1,300 nm. Light from 1,300 nm to 1,700 nm passes through to the bottom Ge cell with minimal interface reflections, owing to the high index of the As$_2$Se$_3$, nearly independent of the thickness of this layer, over a wide range. The 3J and Ge cells operate independently with separate sets of terminals, without electrical crosstalk, thereby eliminating constraints associated with current matching.

Figure 2 and Table 1 present the performance characteristics measured from a completed microcell MJ device (see Methods for details about measurements). The device includes lithographically defined sidewall insulation and lithographically processed metal contacts to the 3J and Ge cells (Fig. 2a). The thin-film geometry of the 3J is beneficial because it allows wafer-level deposition and photolithographic patterning of the interconnections. Current and voltage characteristics measured from the 3J and Ge cells at concentrations ranging from 1 sun (standard AM1.5D spectrum) to ~1,200 suns are shown in Fig. 2b–e. Under 1 sun illumination, the 3J cell and the Ge cell exhibit efficiencies of 32.2% and 0.722% respectively, thus corresponding to a summed efficiency of 32.9%. As the concentration increases, the efficiencies of both cells increase, ultimately reaching maximum values of 42.1% (3J) and 1.81% (Ge) at ~1,000 suns. The maximum total efficiency is 43.9% (Fig. 2f). Measurements of each cell separately with the

Table 1 | Performance of a microscale 3J/Ge cell.

		J_{sc} (mA cm^{-2})	V_{oc} (V)	FF (%)	η (%)	Total η (%)
1 sun	3J cell	14.5	2.64	84.3	32.2	
	Ge cell	6.99	0.181	57.1	0.722	32.9
1,000 suns	3J cell	14,500	3.47	83.7	42.1	
	Ge cell	6990	0.374	69.3	1.81	43.9

other cell in different configurations (open circuit, short circuit and maximum power) show little differences (Supplementary Fig. 24). These results suggest that there is negligible photon or electron coupling between the cells. For concentrations larger than 1,000 suns, the efficiencies decrease primarily as the result of a reduction in the fill factor, probably associated with resistive losses (Fig. 2d,e). Figure 2g quantitatively illustrates, in a manner consistent with experimental data, the external quantum efficiency (EQE) spectra for the integrated MJ device, showing absorption across the entire solar spectrum, from 300 nm to 1,700 nm, with minimal reflection losses. Modelling shows that the reflectance at wavelengths longer than 1,200 nm arises, almost entirely, from limitations of the tri-layer ARC, not from reflection at the interfaces with the As$_2$Se$_3$ (Supplementary Figs 19–23).

For reasons described previously, the interface materials in these systems are critically important. Chalcogenide glasses such as As$_2$Se$_3$ are commonly employed in infrared optics[28,29] but have not been explored for the use reported here. The As$_2$Se$_3$ glass is attractive for present purposes because it offers the ability to form smooth, uniform coatings by simple solution processing, a high resistivity ($10^{10} \sim 10^{12}$ Ω cm) and high electrical breakdown strength (~10^8 V m^{-1}), a refractive index (~2.7) that approaches that of the semiconductors in the cells (~3.4 for GaAs and ~4.3 for Ge at 1,300 nm) and a relatively high thermal conductivity (~1.0 W K^{-1} m^{-1}); see Supplementary Figs 13–16 for details. The role is as an electrically insulating layer to allow independent
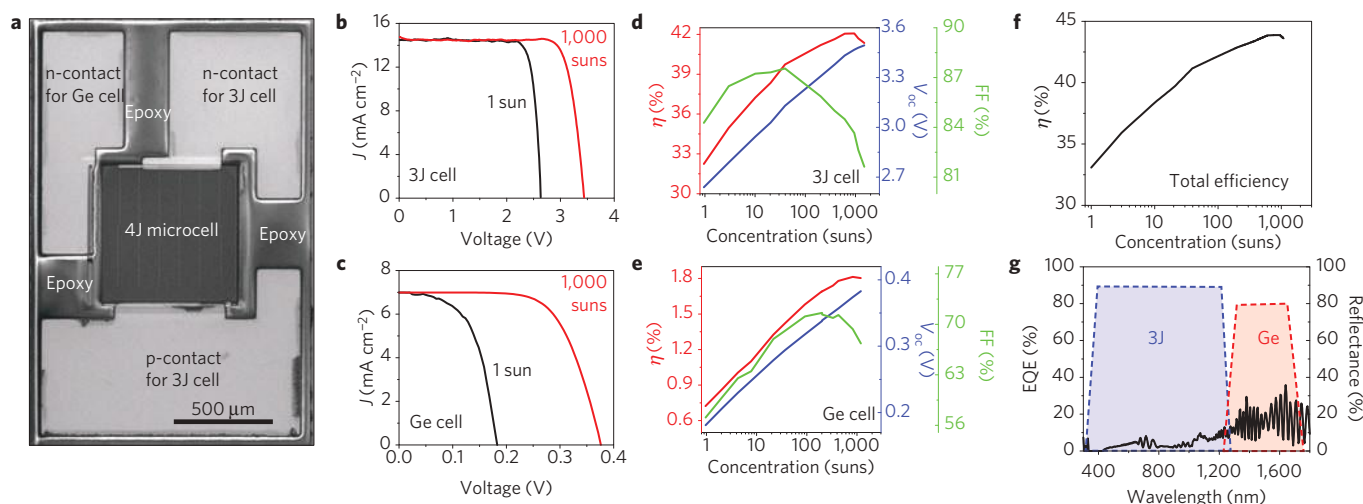
Figure 2 | Image of a packaged quadruple-junction microscale solar cell with separate terminal connections to the top 3J cell and the bottom Ge cell, and key performance parameters. a, SEM image (top view) of an encapsulated and metallized 3J/Ge cell. **b**, Current density (J)–voltage (V) curves for the top 3J cell under 1 sun and 1,000 suns illumination. **c**, J–V curves for the bottom Ge cell under the same conditions. In **b** and **c** the presented J_{sc} values are normalized to an irradiance of 1,000 W m^{-2}. **d**, Cell efficiency (η), open-circuit voltage (V_{oc}) and fill factor (FF) as a function of concentration for the top 3J cell. **e**, η, V_{oc} and FF as a function of concentration for the bottom Ge cell. In **d** and **e** the measured J_{sc} is assumed to be linearly proportional to the irradiance. **f**, Total, summed efficiency as a function of concentration. **g**, Schematic illustrations of the EQE and measurements of the reflectance spectra of a 3J/Ge cell.

operation of the top and bottom cells, with sufficiently high thermal conductivity and index of refraction to minimize barriers to heat transport and losses due to optical reflection, respectively.

Previously explored stacked MJ cells include thick organic adhesives[16–19] and directly bonded interfaces[13–15]. Comparisons of electrical, optical and thermal properties of these cases to those enabled by As$_2$Se$_3$ provide insights into the utility of this material. Figure 3a summarizes the three structures. The thicknesses of the As$_2$Se$_3$ (300 nm) and the organic adhesive (NOA, 10 µm) are chosen to offer sufficient breakdown voltages to support modules with many interconnected cells. Figure 3b presents current–voltage measurements performed by biasing the bottom p-contacts of the 3J cells relative to the top n-contacts of the Ge cells. The direct bond case exhibits a non-insulating interface (~0.1 A at 1 V). Cells with As$_2$Se$_3$ and NOA show leakage currents (~10^{-7} A for As$_2$Se$_3$ and ~10^{-10} A for NOA at up to 20 V) much lower than the photocurrents generated under concentration (~5×10^{-2} A at ~1,000 suns), ensuring that 3J and Ge cells can operate independently in an interconnected network. Measured EQE curves in Fig. 3c indicate that the bottom Ge cell with the As$_2$Se$_3$ interface exhibits responses similar to those in the direct bonded structure, both of which are significantly higher than that of the structure with NOA (index = 1.56). Integrating the EQE over a standard AM1.5D spectrum yields a short-circuit current density (J_{sc}) for the Ge cell with As$_2$Se$_3$ of 7.0 mA cm^{-2}, consistent with the measured J–V curves in Fig. 2c. The Ge cell with NOA exhibits a calculated J_{sc} of 5.3 mA cm^{-2}. This difference is consistent with both the measured optical reflectance spectra from the surfaces of the top 3J cells (Fig. 3d) and the simulated results (Fig. 3e). Thermal properties are also important, especially for operation at high optical concentration. Here, the interface material must not impede dissipation of heat away from the 3J cell. As$_2$Se$_3$ offers significant thermal advantages over the types of organic layers that have been explored in the past. These advantages follow from the combined effects of high breakdown strength, which allows the use of thin-layer geometries, and high thermal conductivity. Figure 3f,g show measured and simulated steady-state temperature distributions at the surfaces of MJ cells

during illumination with a laser beam (488 nm, 0.15 W) configured to generate a thermal power density in the cell area similar to that from irradiance at ~1,000 suns. The results suggest that the As$_2$Se$_3$ interface provides a thermal conductance (3×10^6 W K^{-1}) comparable to the direct bond interface, whereas the thermal conductance for the NOA interface is much lower (10^4 W K^{-1}). The maximum temperatures associated with the As$_2$Se$_3$, direct bond and NOA structures are 39 °C, 38 °C and 68 °C, respectively, consistent with numerical simulations (see Supplementary Figs 26,27 for details). The reduced temperatures improve performance and long-term reliablity[2].

The four-terminal MJ microscale cells can be integrated with dual-stage imaging optics (Fig. 4a,b) based on a moulded primary lens and a secondary, miniature ball lens. Ray tracing results (Fig. 4c,d) show that such a system provides geometric concentration ratios greater than 1,000 and a uniform irradiance distribution on the cell surface[30]. In tests under direct sunlight in North Carolina (Air Mass condition 1.8), the four-terminal photovoltaic module exhibits an efficiency of 33.4% for the 3J cell and 1.0% for the Ge cell, reaching a total efficiency of 34.4% (Fig. 4e). The total module efficiency adjusted to standard test conditions (at cell temperature 25 °C) is 36.5% (see Supplementary Figs 28 and 29 for details). Matching networks enable two-terminal operation, for practical applications[17]. Figure 4f,g present two circuit designs, one that that uses a voltage-matched array with ten MJ cells and another that exploits a current-matched array with three MJ cells. Experiments using related cells demonstrate the effectiveness of these network architectures and validate the methods for calculation (see Supplementary Fig. 35). Experimentally measured performance variation data for separate 3J and Ge cells allow statistical prediction of output currents, voltages and powers associated with the proposed circuit networks (see Supplementary Figs 30–34 for details). The results show that efficiencies of 35.9 ± 0.2% and 36.2 ± 0.3% are possible with current and voltage matching, respectively.

The results presented here clearly demonstrate that printing-based assembly of epitaxially released, MJ thin films with optimized interface materials provides microscale solar cells configured for use with miniaturized concentration optics and matching networks
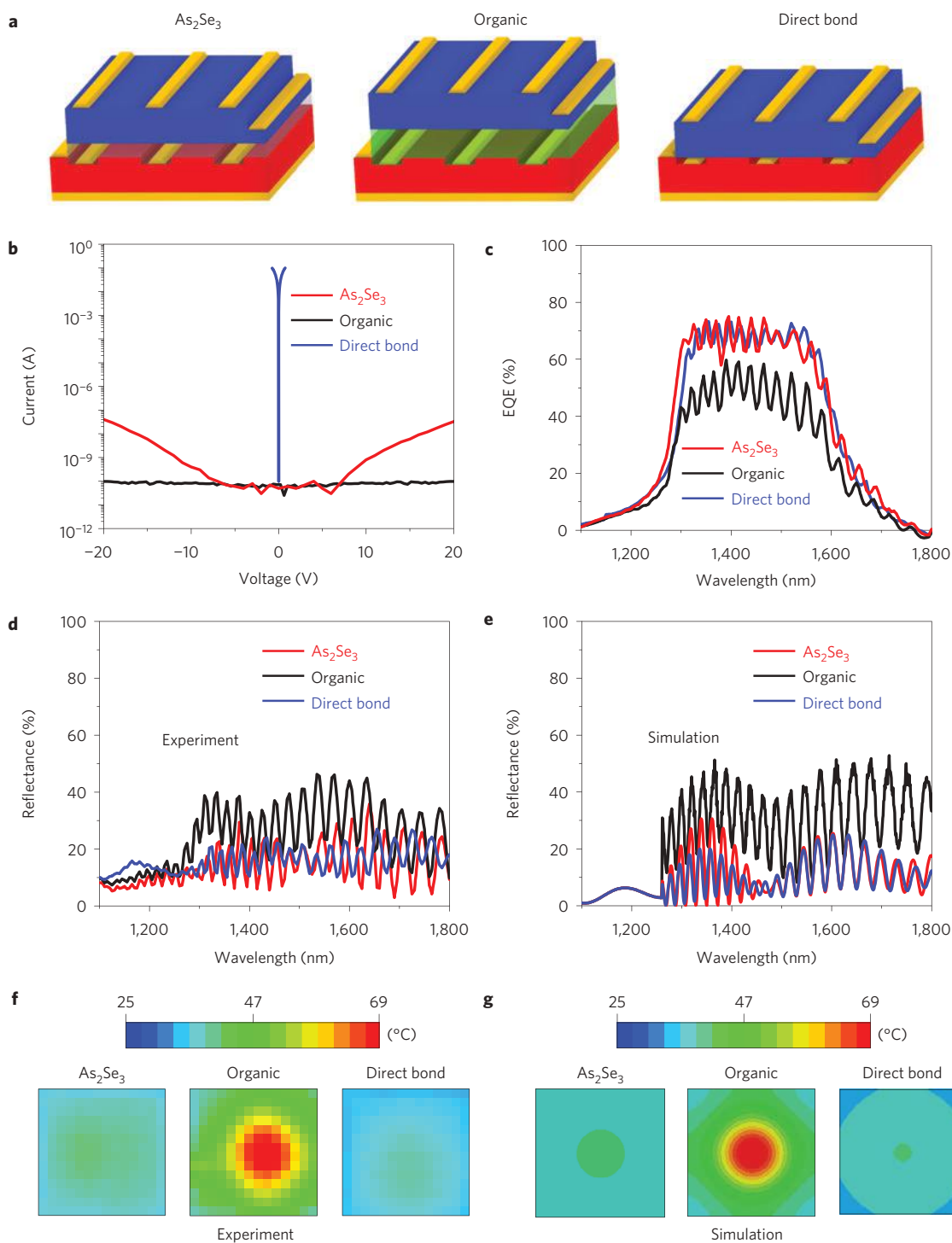
Figure 3 | Schematic illustrations of microscale quadruple-junction structures assembled by printing with different interfaces, and comparisons of their electrical, optical and thermal properties. a, Schematic illustrations of stacked 3J/Ge cells with different interfaces (300 nm As_2Se_3, 10 μm organic adhesive (NOA), and direct bond). **b**, Leakage currents measured between the bottom contact of the top 3J cell and the top contact of the bottom Ge cell, as a function of applied voltage. **c**, EQE spectra measured from the Ge cells. **d,e**, Measured and simulated infrared reflectance spectra, respectively. **f,g**, Measured and simulated temperature distributions, respectively, associated with irradiation of the structures with a laser beam (centre wavelength 488 nm, 0.15 W). Map size: 650 μm × 650 μm.

to yield ultrahigh-efficiency module-level photovoltaics. These schemes can also apply immediately to more advanced systems, including those that involve increased numbers of junctions and/or stacking operations. Some possibilities are five- or even six-junction cells, for which practical efficiencies might reach more than 45%. Straightforward improvements in the concentration optics

(for example, addition of ARC layers on the primary lens would achieve an additional ~1% efficiency boost) and enhancements to the ARC on the cell surface can lead to further increases in module performance. Other types of chalcogenide glasses with refractive indices ($n > 3.0$) higher than As_2Se_3 can also be considered[29]. Collectively, these and other readily achievable enhancements

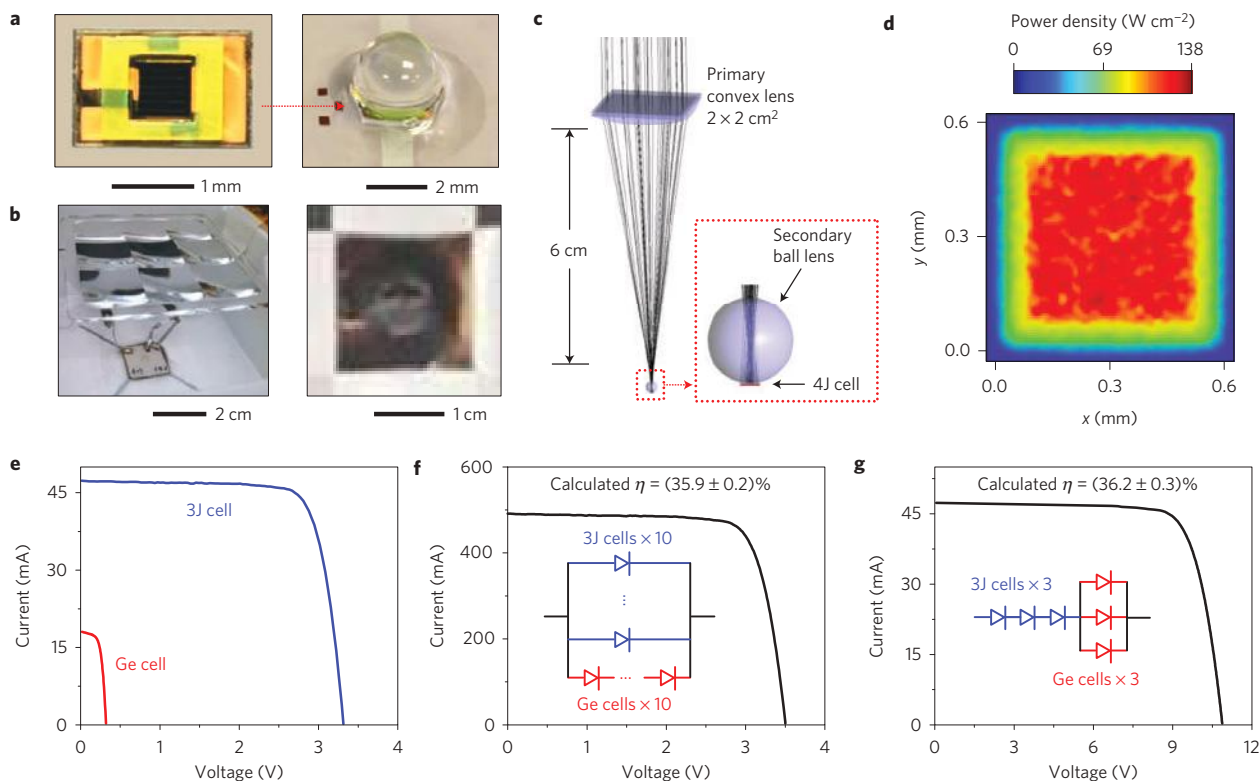**Figure 4 | Images and performance of completed quadruple-junction microscale solar cells with concentration optics. a**, Optical images of a diced stacked cell (left) and a cell with a secondary ball lens (right). **b**, Side view (left) and top view (right) of a cell in a module with a secondary ball lens and a primary lens. **c**, Ray tracing analysis of a fully integrated module. **d**, Calculated irradiance distribution under the incidence of the AM1.5D spectrum (power 1,000 W m^{-2}). **e**, Current (I)–voltage (V) curves of the module measured under direct exposure to sunlight. Measurements were taken at 13:09 on 14 November 2013 in Durham, North Carolina, USA. Air Mass condition is 1.8. **f**, Theoretically predicted I–V curve of a voltage-matched array with ten interconnected cells. **g**, Theoretically predicted I–V curve of a current-matched array with three interconnected cells. Insets show circuit diagrams.

suggest promising paths to photovoltaic systems that use the entire solar spectrum and approach the thermodynamic limits in efficiency.

Methods

Device fabrication. The 3J (InGaP/GaAs/InGaAsNSb) cell is epitaxially grown on a lattice-matched GaAs substrate[7], with a total thickness of ∼10 μm that includes the active materials and a GaAs current-spreading layer several micrometres thick beneath them as well as a sacrificial layer of AlInP (ref. 24). An anti-reflective coating (90 nm SiO$_2$/45 nm Si$_3$N$_4$/30 nm TiO$_2$) deposited on the 3J cell minimizes reflection losses. The diffused-junction Ge cell is based on a 230 μm p-Ge wafer with a lattice-matched n-GaAs epitaxial film (1.5 μm) as a transparent contact layer. Metal layers (Ge/Ni/Au) serve as contacts in recessed geometries. The cell active area (600 × 600 μm^2), which is defined by the photomasks used in lithographic process, is measured directly after fabrication. To minimize the effects of shadowing, the metal contact lines in both the 3J and the Ge cells adopt the same layout and are aligned to one another at the printing step. A solution of As$_2$Se$_3$ (powder from Alfa Aesar) dissolved in ethylenediamine (concentration 0.2 g ml^{-1}) is spin cast on the Ge cells, to form, on curing at 150 °C for 10 h in an inert atmosphere, a 300 nm thick As$_2$Se$_3$ glass film[27]. An ultrathin (10 nm) adhesive layer (InterVia 8023-10) spin coated on the As$_2$Se$_3$ improves the printing yields. Etching the AlInP layer in hydrochloric acid[24] releases the 3J cells to enable their printing onto the As$_2$Se$_3$-coated Ge cells with the ultrathin adhesive. This process uses a poly(dimethylsiloxane) stamp mounted in an automated set of equipment for aligning and printing[26] 100 cells, or more, in a single step. The same printing process can produce structures with NOA (NOA61, by Norland Products, spin coated on bare Ge cells) and direct bond (no adhesive, printing followed by heating at ∼115 °C for 10 min) interfaces. The adhesion strength between the 3J cells and Ge cells for the case of As$_2$Se$_3$ is >200 kPa. The printed 3J/Ge MJ cells are encapsulated in an epoxy layer (InterVia 8023-10, thickness 10 μm) and metallized to form contact pads. Thermal cycling tests (rapid heating at 110 °C for 1 min and cooling at 20 °C for 1 min, 10 cycles) reveal no changes in the mechanical, optical, electrical or photovoltaic characteristics of the devices (Supplementary Fig. 10).

Device measurements. A four-probe set-up allows evaluation of current–voltage responses. A solar simulator (Oriel 91192) with an AM1.5D filter yields 1 sun illumination. EQE and reflectance spectra are measured using a spectroradiometer system. Measurements of short-circuit current density (J_{sc}) under blanket, 1 sun illumination are consistent with those that involve integration of EQE measurements using an illuminating beam with a known area, smaller than that of the cell. Such EQE measurements provide a method for calculating concentrator cell efficiency that does not require precise measurement of the active cell area. Coupling light from a Xenon arc lamp through an optical fibre and a set of lenses yields concentrated illumination. The irradiance power is assumed to be linearly proportional to the measured short-circuit current (I_{sc}). The concentration ratios are computed from the measured currents, using an active cell area of 600 μm × 600 μm. The actual cell area involves slight uncertainties due to processing effects, such as different etching rates of the various sub-cells. These effects appear as uncertainties in the computed concentration ratios. The measurements taken under direct exposure to sunlight for the integrated solar module were taken at 13:09 on 14 November 2013 in Durham, North Carolina, USA. Air Mass condition is 1.8.

References

1. Breyer, C. & Gerlach, A. Global overview on grid-parity. *Prog. Photovolt. Res. Appl.* **21,** 121–136 (2013).
2. Luque, A. & Hegedus, S. *Handbook of Photovoltaic Science and Engineering* (Wiley, 2011).
3. Polman, A. & Atwater, H. A. Photonic design principles for ultrahigh-efficiency photovoltaics. *Nature Mater.* **11,** 174–177 (2012).
4. Green, M. A., Emery, K., Hishikawa, Y., Warta, W. & Dunlop, E. D. Solar cell efficiency tables (version 43). *Prog. Photovolt. Res. Appl.* **22,** 1–9 (2014).
5. Shockley, W. & Queisser, H. J. Detailed balance limit of efficiency of p–n junction solar cells. *J. Appl. Phys.* **32,** 510–519 (1961).
6. Luque, A. Will we exceed 50% efficiency in photovoltaics? *J. Appl. Phys.* **110,** 031301 (2011).

7. Derkacs, D., Jones-Albertus, R., Suarez, F. & Fidaner, O. Lattice-matched multijunction solar cells employing a 1 eV GaInNAsSb bottom cell. *J. Photon. Energy* **2,** 021805 (2012).

8. King, R. R. *et al.* 40% efficient metamorphic GaInP/GaInAs/Ge multijunction solar cells. *Appl. Phys. Lett.* **90,** 183516 (2007).

9. Geisz, J. F. *et al.* High-efficiency GaInP/GaAs/InGaAs triple-junction solar cells grown inverted with a metamorphic bottom junction. *Appl. Phys. Lett.* **91,** 023502 (2007).

10. King, R. R. *et al.* Band-gap-engineered architectures for high-efficiency multijunction concentrator solar cells. *Proc. 24th Euro. Photovolt. Solar Energy Conf.* 55–61 (2009).

11. Wojtczuk, S. *et al.* 42% 500X bi-facial growth concentrator cells. *AIP Conf. Proc.* **1407,** 9–12 (2011).

12. Sasaki, K. *et al.* Development of InGaP/GaAs/InGaAs inverted triple junction concentrator solar cells. *AIP Conf. Proc.* **1556,** 22–25 (2013).

13. Tanabe, K., Watanabe, K. & Arakawa, Y. III-V/Si hybrid photonic devices by direct fusion bonding. *Sci. Rep.* **2,** 349 (2012).

14. Derendorf, K. *et al.* Fabrication of GaInP/GaAs//Si solar cells by surface activated direct wafer bonding. *IEEE J. Photovolt.* **3,** 1423–1428 (2013).

15. Dimroth, F. Wafer bonded four-junction GaInP/GaAs/GaInAsP/GaInAs concentrator solar cells with 44.7% efficiency. *Prog. Photovolt. Res. Appl.* **22,** 277–282 (2014).

16. Gee, J. M. & Virshup, G. F. A 31% efficient GaAs/silicon mechanically stacked, multijunction concentrator solar cell. *Proc. 20th IEEE Photovolt. Spec. Conf.* **1,** 754–758 (1988).

17. Fraas, L. M. *et al.* Over 35% efficient GaAs/GaSb stacked concentrator cell assemblies for terrestrial applications. *Proc. 21st IEEE Photovolt. Spec. Conf.* **1,** 190–195 (1990).

18. Takamoto, T. *et al.* InGaP/GaAs and InGaAs mechanically-stacked triple-junction solar cells. *Proc. 26th IEEE Photovolt. Spec. Conf.* 1031–1034 (1997).

19. Zhao, L., Flamand, G. & Poortmans, J. Recent progress and spectral robustness study for mechanically stacked multi-junction solar cells. *AIP Conf. Proc.* **1277,** 284–289 (2010).

20. Barnett, A. *et al.* Very high efficiency solar cell modules. *Prog. Photovolt. Res. Appl.* **17,** 75–83 (2009).

21. Green, M. A. & Ho-Baillie, A. Forty three percent composite split-spectrum concentrator solar cell efficiency. *Prog. Photovolt. Res. Appl.* **18,** 42–47 (2010).

22. McCambridge, J. D. *et al.* Compact spectrum splitting photovoltaic module with high efficiency. *Prog. Photovolt. Res. Appl.* **19,** 352–360 (2011).

23. Yoon, J. *et al.* GaAs photovoltaics and optoelectronics using releasable multilayer epitaxial assemblies. *Nature* **465,** 329–333 (2010).

24. Meitl, M. *et al.* Materials and processes for releasing printable compound semiconductor devices. WIPO patent WO 2012018997A2 (2012).

25. Posthuma, N. E., van der Heide, J., Flamand, G. & Poortmans, J. Emitter formation and contact realization by diffusion for germanium photovoltaic devices. *IEEE Trans. Electron. Dev.* **54,** 1210–1215 (2007).

26. Carlson, A., Bowen, A. M., Huang, Y., Nuzzo, R. G. & Rogers, J. A. Transfer printing techniques for materials assembly and micro/nanodevice fabrication. *Adv. Mater.* **24,** 5284–5318 (2012).

27. Zou, Y. *et al.* Effect of annealing conditions on the physio-chemical properties of spin-coated As₂Se₃ chalcogenide glass films. *Opt. Mater. Express* **2,** 1723–1732 (2013).

28. Popescu, M. A. *Non-Crystalline Chalcogenides* (Kluwer Academic Publishers, 2002).

29. McBrearty, E. J. *et al.* Chalcogenide glass films for the bonding of GaAs optical parametric oscillator elements. *Proc. SPIE* **5273,** 430–439 (2003).

30. Menard, E. *et al.* Optics development for micro-cell based CPV modules. *Proc. SPIE* **8108,** 810805 (2011).

Author contributions

X.S., C.A.B., S.B., M.M., H.Y., L.S., A.R.B., C.J.C. and J.A.R. designed and fabricated the devices. X.S., C.A.B., J.W.W., B.F., L.S., A.R.B. and C.J.C. measured the data. X.S., B.F., M.M. and S.W. performed simulations. R.G.N., S.B. and J.A.R. provided guidance. X.S., C.A.B., M.M. and J.A.R. wrote the paper.

Additional information

Supplementary information is available in the online version of the paper. Reprints and permissions information is available online at www.nature.com/reprints. Correspondence and requests for materials should be addressed to S.B. or J.A.R.

Competing financial interests

The authors declare that C.A.B., S.B., J.W.W., B.F., M.M., H.Y., S.B. and J.A.R. (affiliated with Semprius and Solar Junction) are involved in commercializing various technologies related to those described here. J.A.R. is a co-founder of Semprius.

Printing-based assembly of quadruple-junction four-terminal microscale solar cells for the realization of high-efficiency modules

Xing Sheng,[1][†] Christopher A. Bower,[2][†] Salvatore Bonafede,[2] John W. Wilson,[2] Brent Fisher,[2] Matthew Meitl,[2] Homan Yuen,[3] Shuodao Wang,[1] Ling Shen,[4] Anthony R. Banks,[5] Christopher J. Corcoran,[6] Ralph G. Nuzzo,[1, 6] Scott Burroughs,[2*] and John A. Rogers[1, 6*]

[1]*Department of Materials Science and Engineering, University of Illinois at Urbana-Champaign, Urbana, IL 61801, USA*

[2]*Semprius, Inc., Durham, NC 27713, USA*

[3]*Solar Junction, San Jose, CA 95131, USA*

[4]*Department of Physics, College of Sciences, China University of Mining and Technology, Xuzhou, Jiangsu 221116, P.R. China*

[5]*Department of Physics, University of Illinois at Urbana-Champaign, Urbana, IL 61801, USA*

[6]*Department of Chemistry, University of Illinois at Urbana-Champaign, Urbana, IL 61801, USA*

[†]These authors contributed equally to this work.

[*]Correspondence should be addressed to: jrogers@illinois.edu and scott.burroughs@semprius.com
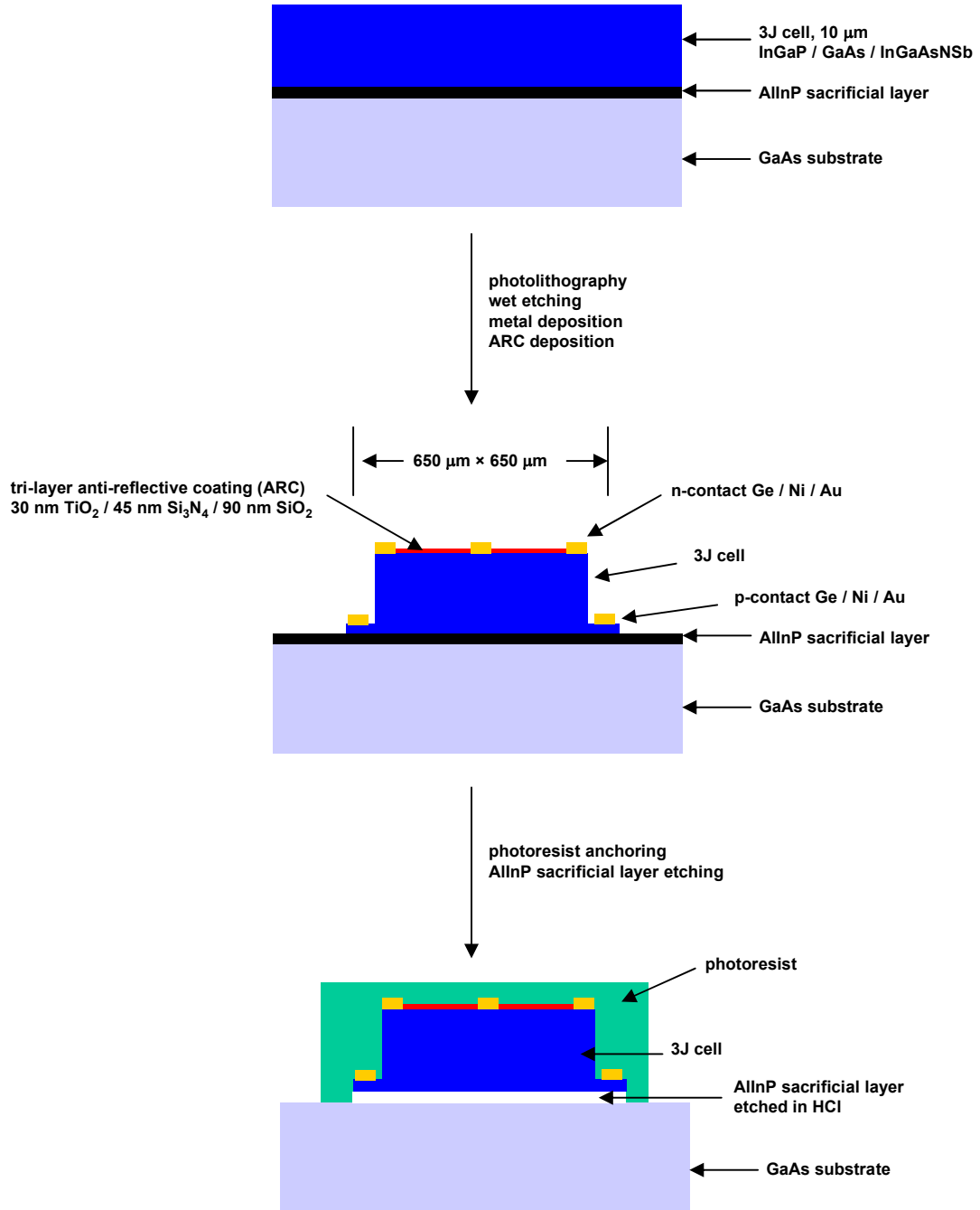
Figure S1. Process flow for fabricating 3J cells on a GaAs substrate with a releasable AlInP sacrificial layer.
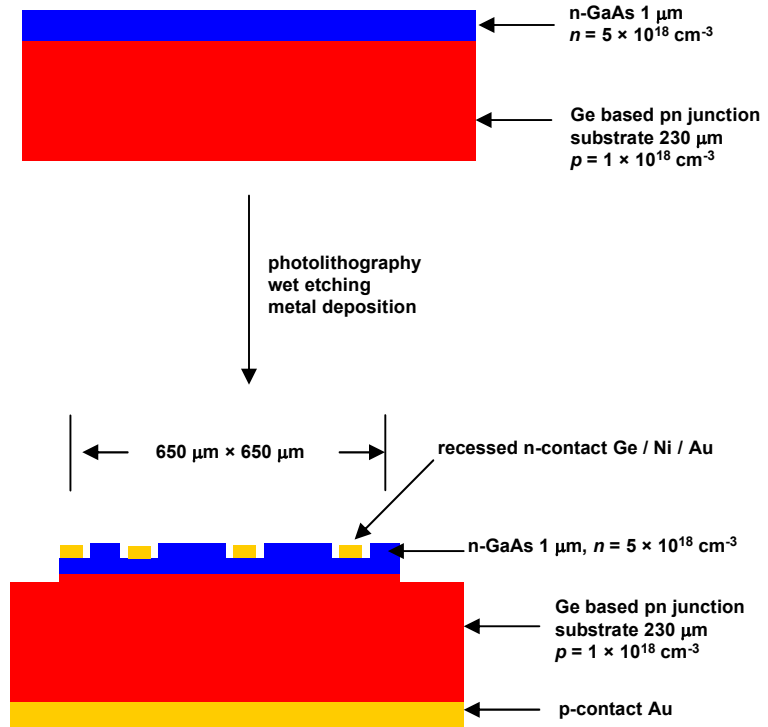
Figure S2. Process flow for fabricating Ge cells.
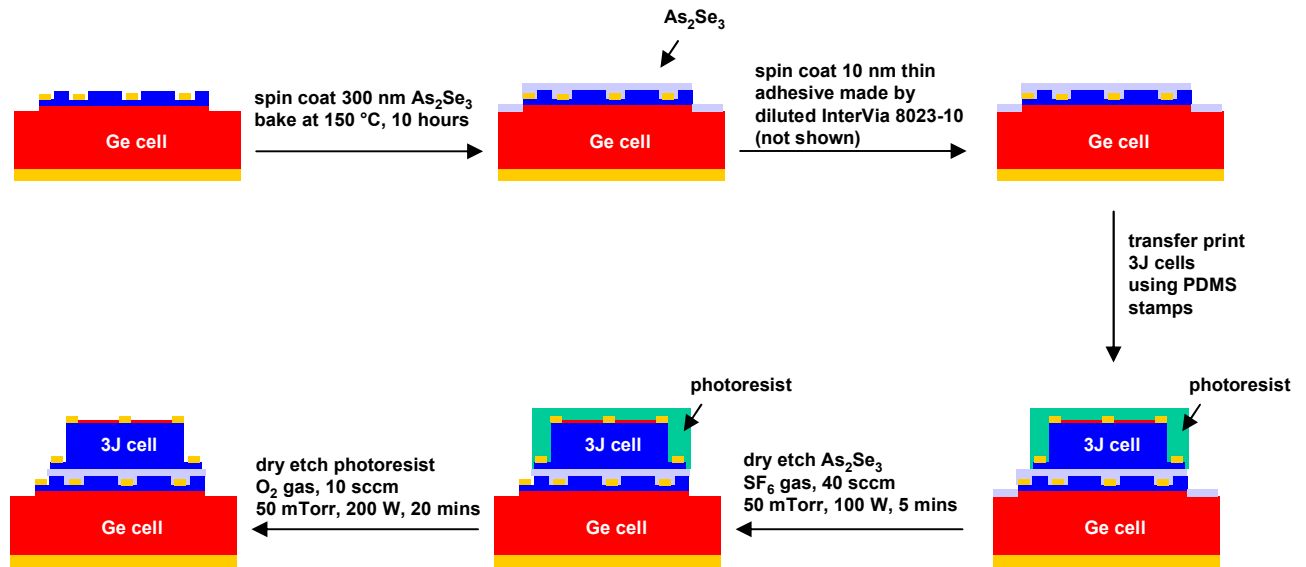
Figure S3. Process flow for fabricating 3J/Ge cells by transfer printing.
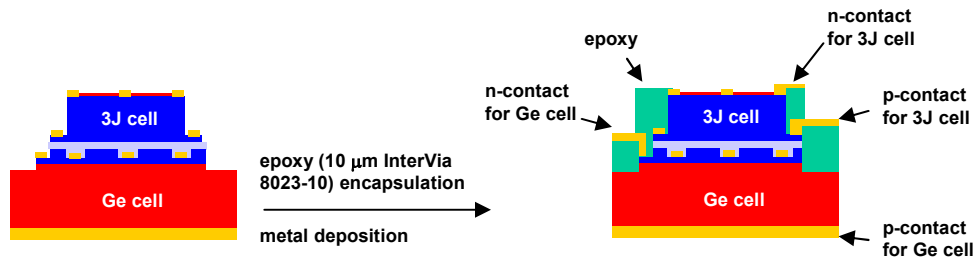
Figure S4. Schematic illustration for encapsulating assembled 3J/Ge cells in epoxy and metal deposition for contact pads
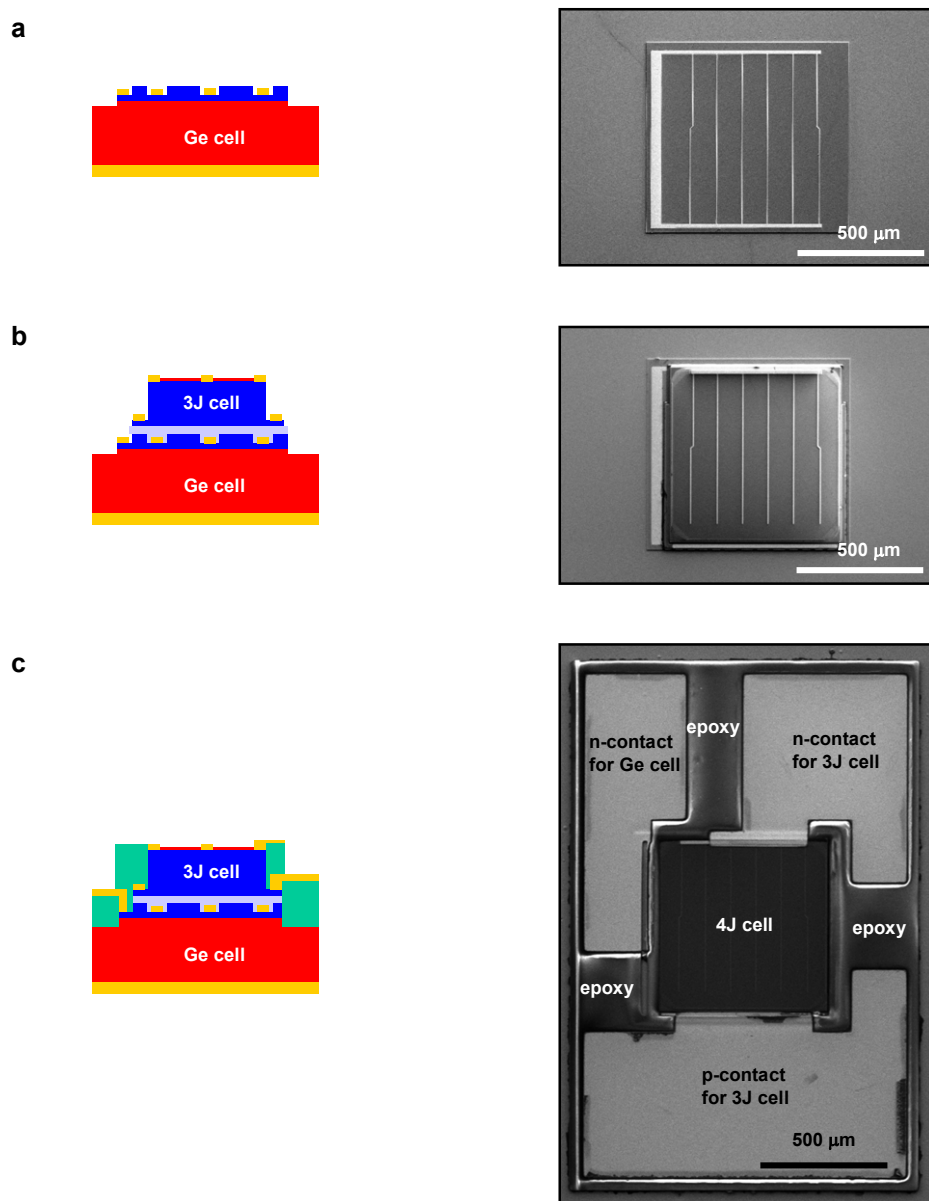
Figure S5. Schematic illustrations and SEM images of (a) a bare Ge cell, (b) a assembled 3J/Ge cell, and (c) an encapsulated 3J/Ge cell with metal contact pads.

a

Si wafer → spin coat SU8-50 photolithography →

SU8 holes
thickness 0.1 mm
size 0.6 mm x 0.6 mm
spacing 0.6 mm x 1.2 mm

Si wafer → pour PDMS (5:1 monomer:catalyst)

cure 75 °C for 2 hours →

PDMS

Si wafer → peel off → PDMS

b

5 mm

c

Backing layer

Post

200 µm
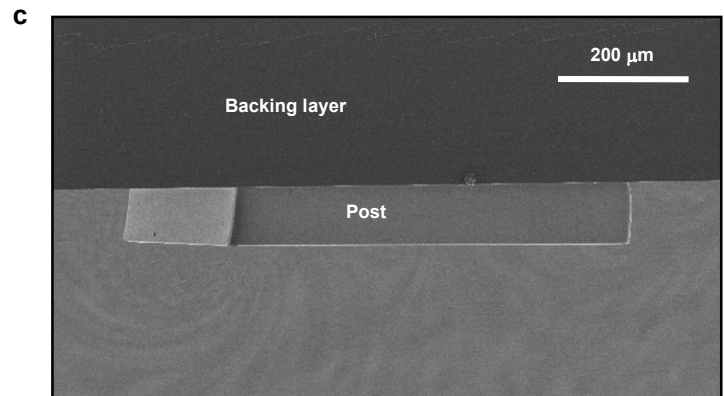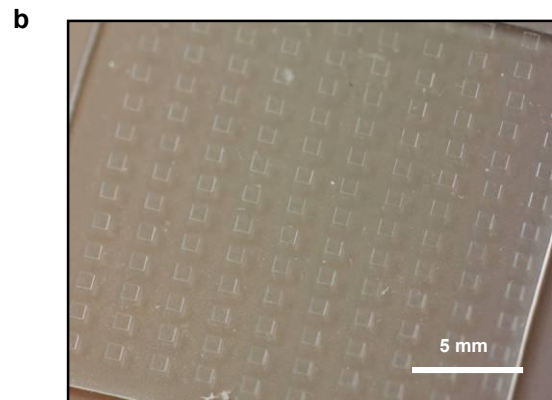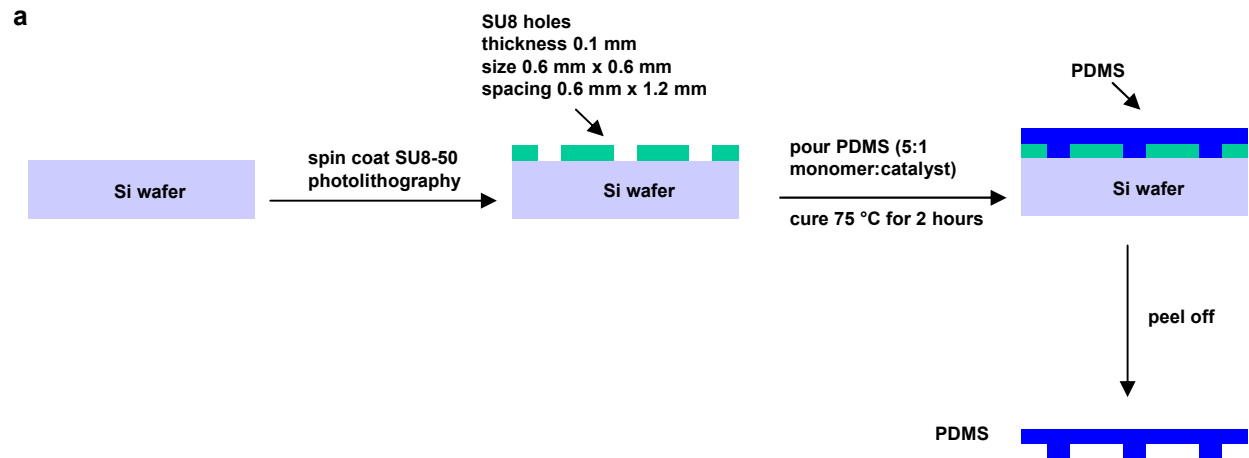
Figure S6. (a) Process flow for fabricating PDMS stamps. (b) Optical image of a PDMS stamp with a 10 × 10 post array. (c) SEM image of the PDMS stamp, including post and backing layer.
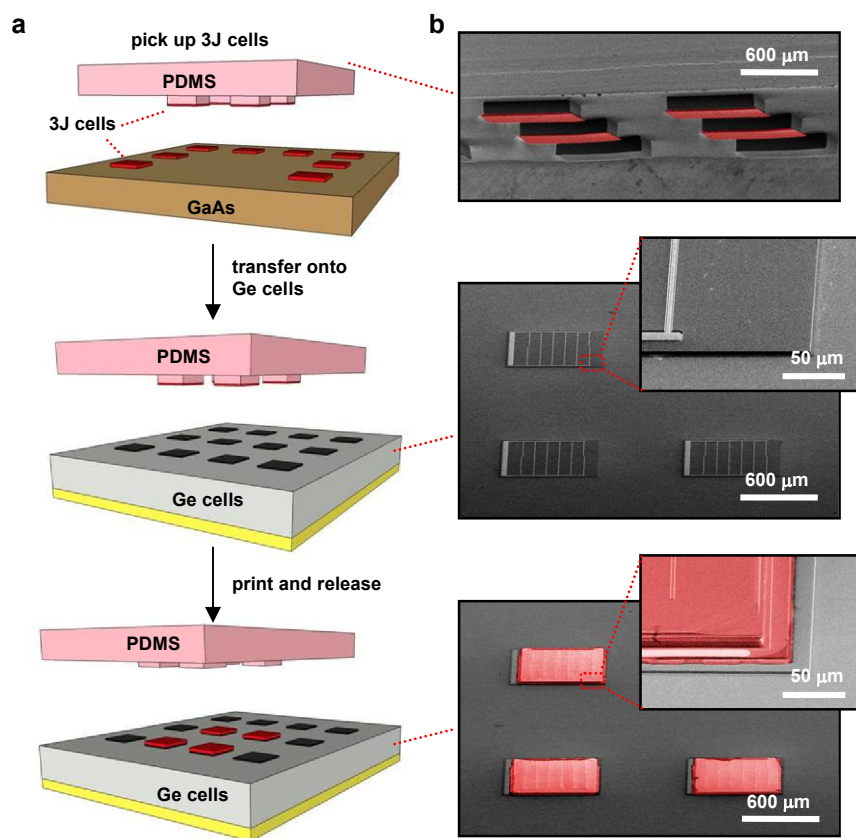
Figure S7. (a) Process flow for fabricating assembled 3J/Ge cells using transfer printing. (b) SEM images (side view) of PDMS stamps with 3J cells, bare Ge cells and printed 3J/Ge cells. Images for 3J cells are colorized. Insets show magnified view of the cell structures. Reference for printing method: Carlson, A. *et al.* Shear-enhanced adhesiveless transfer printing for use in deterministic materials assembly. *Appl. Phys. Lett.* **98,** 264104 (2011).
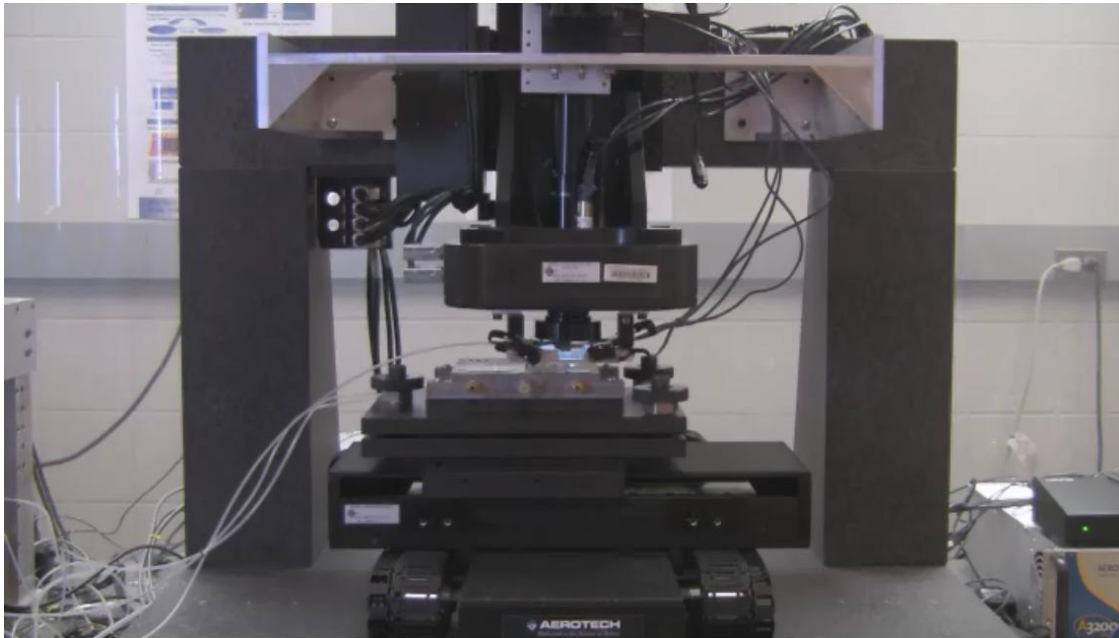
Figure S8. A photograph of the printing machine used to assemble the 3J/Ge solar cells. Reference on parallel, wafer-scale transfer printing process: Justice, J. *et al.* Wafer-scale integration of group III–V lasers on silicon using transfer printing of epitaxial layers. *Nature Photonics* **6,** 610–614 (2012).

a

b
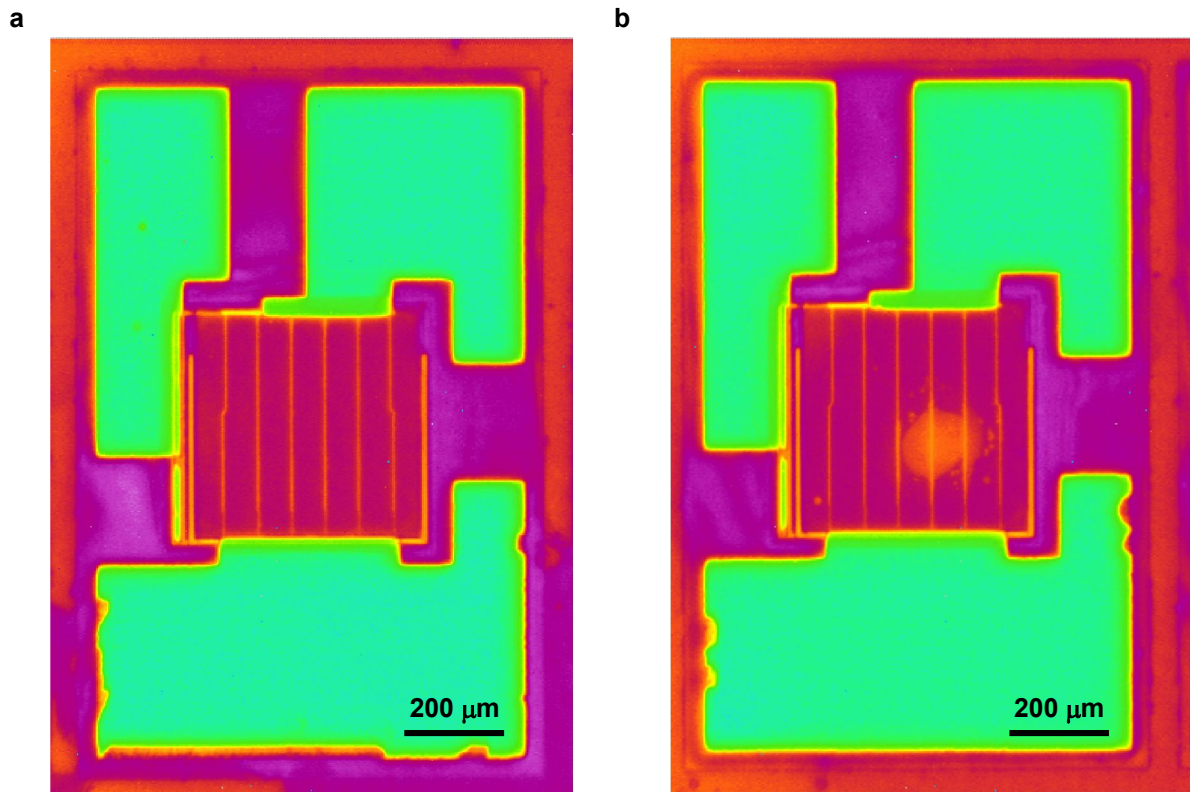
Figure S9. Colorized infrared optical images of two assembled 3J/Ge cells with As$_2$Se$_3$ interface. Different colors indicate the difference in emissivity. (a) A cell with a perfectly bonded interface; (b) A cell exhibiting air voids due to unwanted particles at the interface during the printing process.
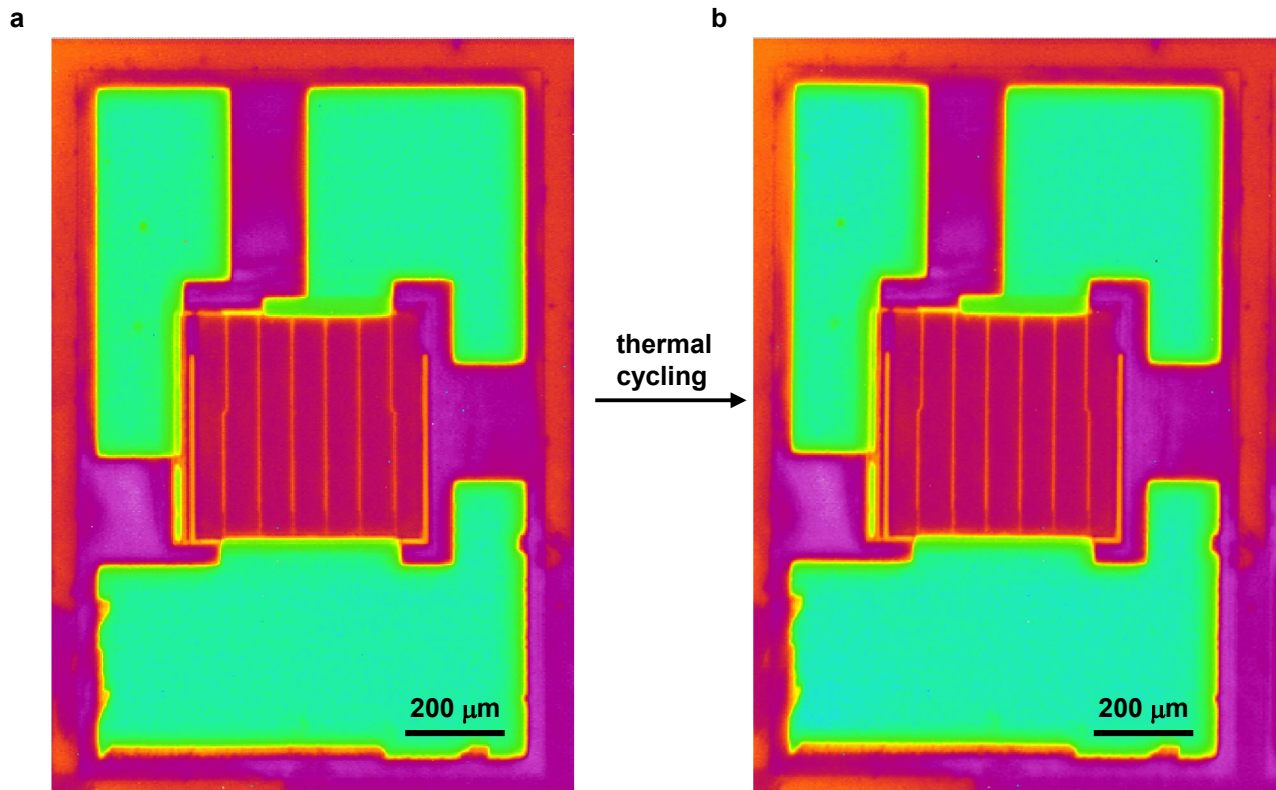
Figure S10. Colorized infrared optical images of an assembled 3J/Ge cell with As$_2$Se$_3$ interface, (a) before and (b) after thermal cycling. Different colors indicate the difference in emissivity. The thermal cycling is performed by rapid heating (at 110 °C for 1 min on a hot plate) and cooling (at 20 °C for 1 min on a cold plate) for 10 cycles. No interface and performance degradations are observed.
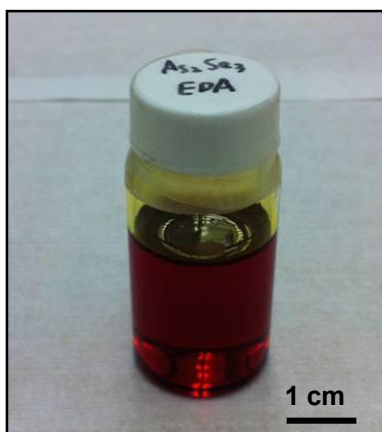
Figure S11. Optical image of a bottle with As$_2$Se$_3$ dissolved into ethylenediamine solution (0.2 g/mL).

a

3J cell

back surface of 3J cell
RMS roughness = 0.12 nm

b

front surface of As$_2$Se$_3$ coated Ge cell
RMS roughness = 1.0 nm
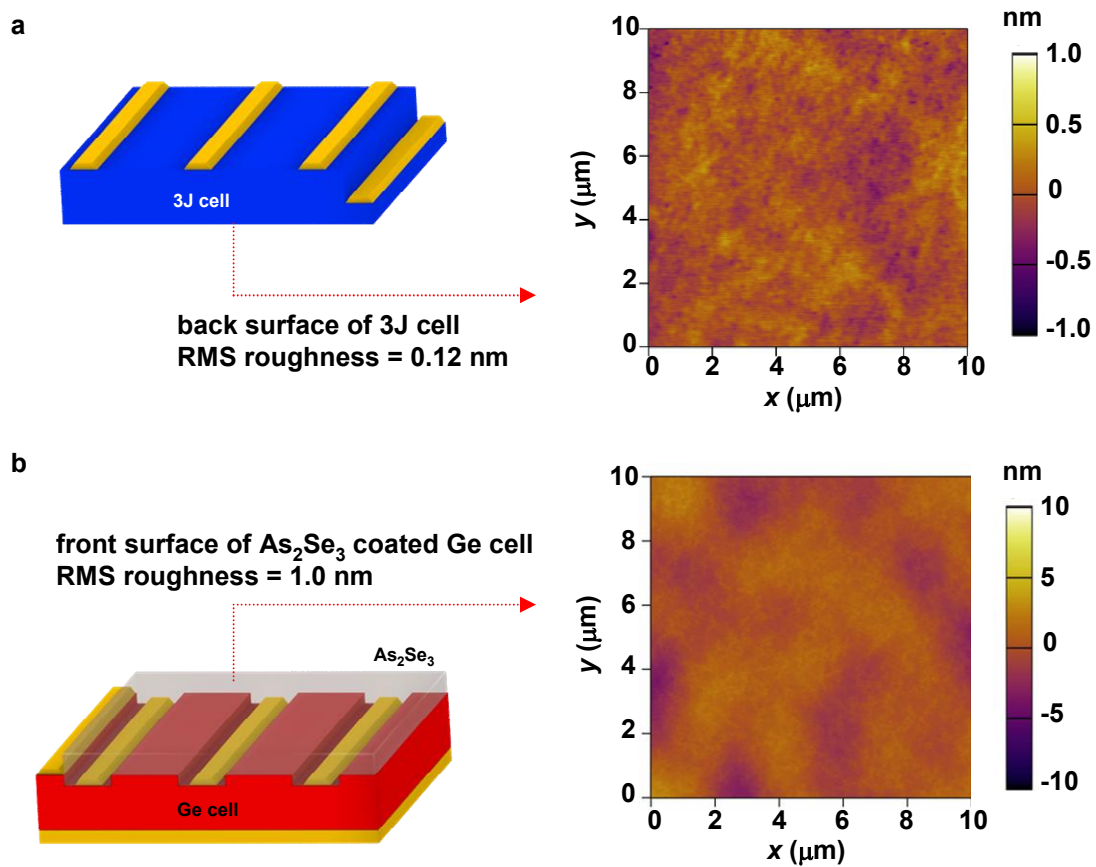
As$_2$Se$_3$

Ge cell

Figure S12. (a) AFM image of the back surface of a 3J cell. Measured RMS roughness 0.12 nm. (b) AFM image of a 300 nm As$_2$Se$_3$ film coated on a Ge cell. Measured RMS roughness 1.0 nm.
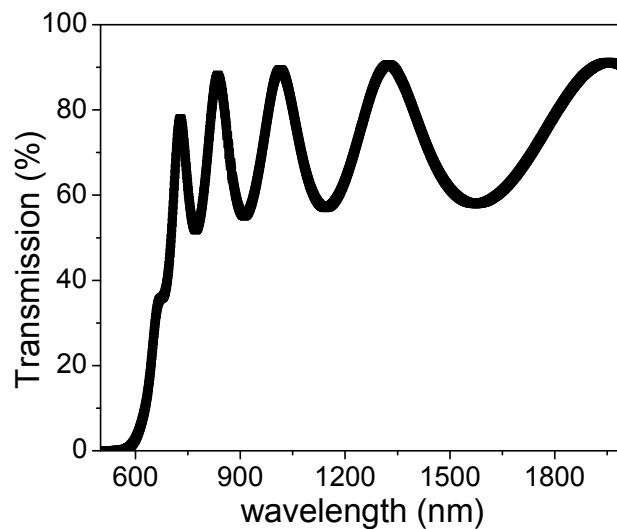
Figure S13. Measured transmission spectrum of a 807 nm thick As_2Se_3 film coated on 1 mm thick glass. The measured refractive index for As_2Se_3 from 900 nm to 2000 nm is 2.67. Calculation is based on the method in: Swanepoel, R. Determination of the thickness and optical constants of amorphous silicon. *J. Phys. E: Sci. Instrum.* **16,** 1214–1222 (1983).
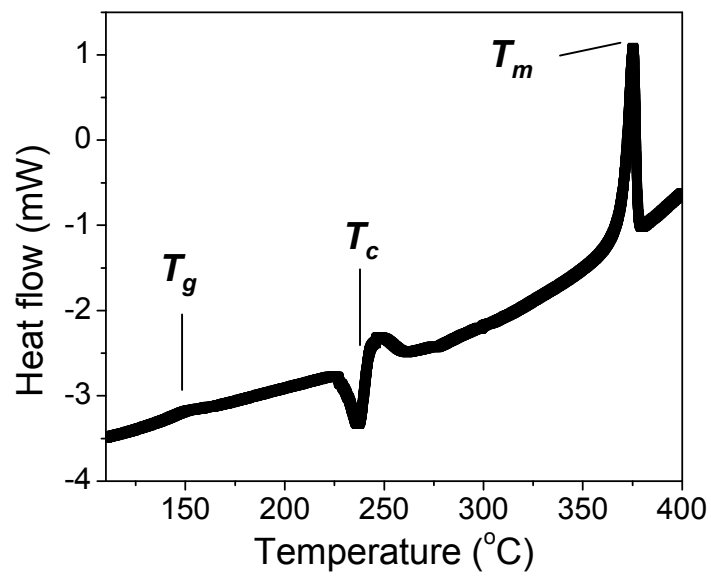
Figure S14. Differential scanning calorimetric (DSC) curve of As_2Se_3 films, showing glass transition temperature T_g = 150 °C, crystallization temperature T_c = 250 °C, and melting temperature T_m = 370 °C.
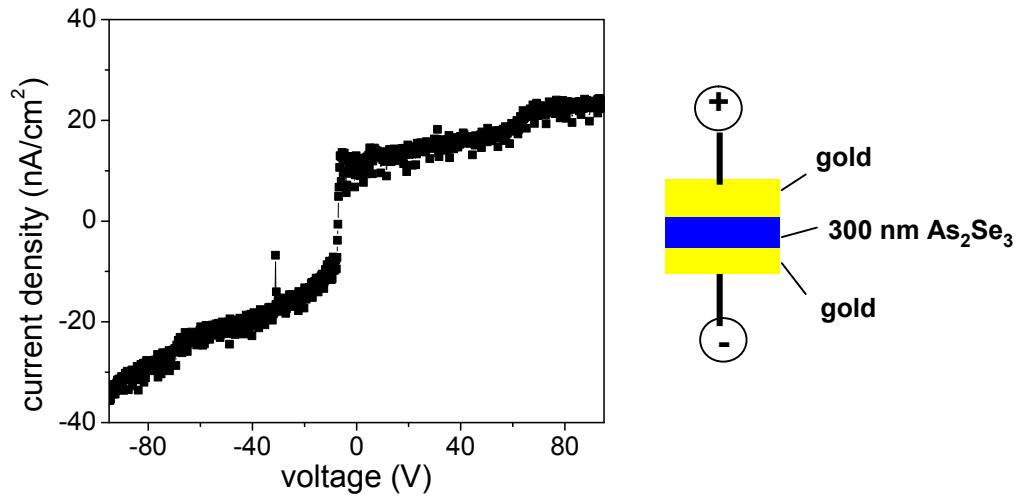
Figure S15. Current-voltage curve of a 300 nm As_2Se_3 film with gold contacts on both sides, measured from -100 V to + 100 V. Measured resistivity is $10^{13} \sim 10^{14}$ Ω*cm.

Refractive index[1]	2.77
Optical bandgap[2]	1.7 eV
Glass transition temperature[2]	180 °C ~ 200 °C
Melting temperature[2]	360 °C
Resistivity[3]	10^{10} ~ 10^{12} Ω·cm
Dielectric strength[4]	~ 10^8 V/m
Thermal conductivity[5]	1.0 W/K/m
Thermal expansion coefficient[6]	6×10^{-5} /K
Young's modulus[7]	15 GPa

Figure S16. Properties of thin-film As_2Se_3 reported in literature.

References:

1. Zou, Y. *et al.* Effect of annealing conditions on the physio-chemical properties of spin-coated As_2Se_3 chalcogenide glass films. *Opt. Mater. Express* **2,** 1723–1732 (2013).
2. Popescu, M. A. *Non-Crystalline Chalcogenides* (Kluwer Academic Publishers, 2002).
3. Adler, D. *Amorphous Semiconductors* (CRC Press, 1971).
4. Fairman, R. & Ushkov, B. *Semiconducting Chalcogenide Glass II Properties of Chalcogenide Glasses* (Elsevier, 2004).
5. Kolomiec, B. T. *et al.* Thermal conductivity of amorphous As_2Se_3 with copper. *Czech. J. Phys. B* **21,** 657–661 (1971).
6. Voronova, A. E., Ananichev, V. A. & Blinov, L. N. Thermal expansion of melts and glasses in the As–Se system. *Glass Phys. Chem.* **27,** 267–273 (2001).
7. Shchurova, T. N. & Savchenko, N. D. Correlation between mechanical parameters for amorphous chalcogenide films. *J. Optoelectron. Adv. Mater.* **3,** 491–498 (2001).
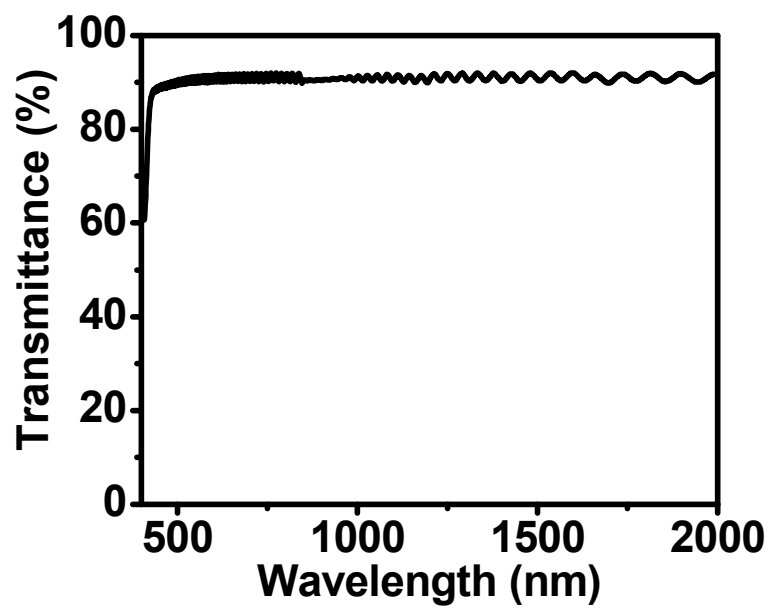
Figure S17. Transmission spectrum of a 10 μm thick InterVia 8023-10 film coated on 1 mm thick glass. The material is transparent above 500 nm, and has a refractive index of 1.56.

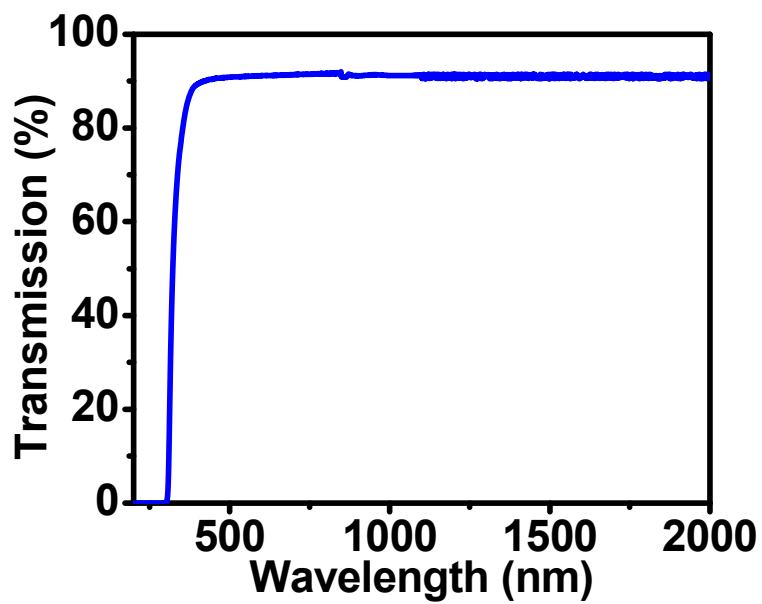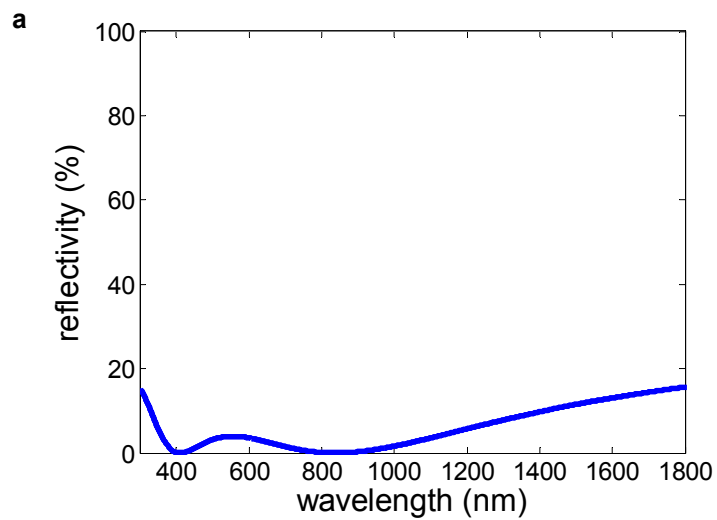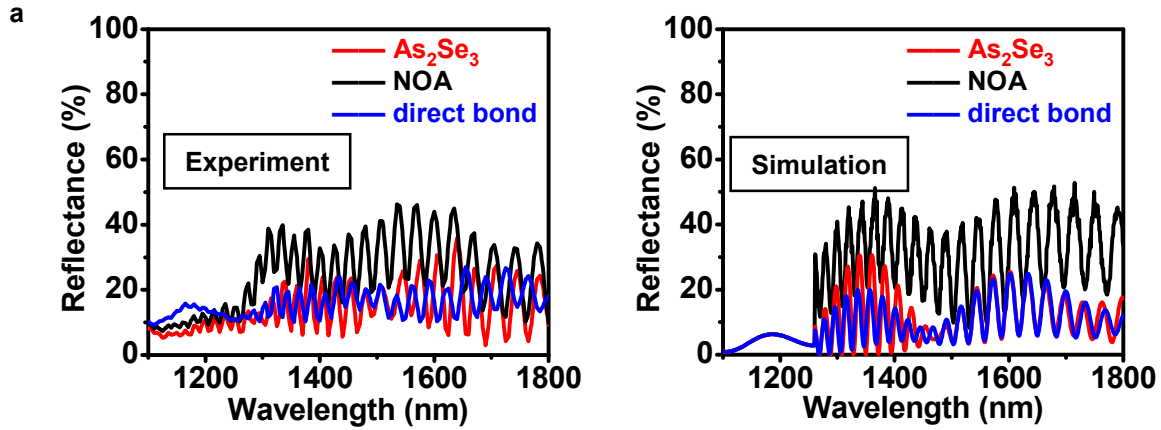**Figure S18.** Measured transmission spectrum of NOA 61 (300 μm free standing film) by Norland Products Inc. Further information can be found in: https://www.norlandprod.com/adhesives/noa%2061.html

a

b

Material	Index	Thickness
air	1.0	infinite
SiO_2	1.45	90 nm
Si_3N_4	2.0	45 nm
TiO_2	2.3	30 nm
GaAs	3.5	infinite

Figure S19. (a) Simulated reflection spectrum of a tri-layer ARC coated on GaAs. (b) Layer structure used in the simulation.

a

Material		Index	Thickness
air		1.0	infinite
SiO$_2$		1.45	90 nm
Si$_3$N$_4$		2.0	45 nm
TiO$_2$		2.3	30 nm
GaAs		3.6	10 μm
interface	As$_2$Se$_3$	2.7	300 nm
	NOA	1.56	10 μm (incoherent)
	direct bond	-	-
GaAs		3.6	1.0 μm
Ge		4.3	infinite

Figure S20. (a) Measured and simulated reflection spectra for assembled 3J/Ge cells with different interfaces (also shown in Fig. 3d and 3f). (b) Layer structure used in the simulation. A 10 μm thick GaAs layer is used in the simulation model to replace the actual 3J cell structure. Note that the 10 μm thick NOA layer is assumed to generate incoherent interference, due to the thickness non-uniformity. Transfer matrix method is used. Reference: Troparevsky, M. C. Transfer-matrix formalism for the calculation of optical response in multilayer systems: from coherent to incoherent interference. *Opt. Express* **18,** 24715-24721 (2010). Details on the optical properties of different materials can be found in: Palik, E. *Handbook of optical constants of solids* (Academic Press, 1998).
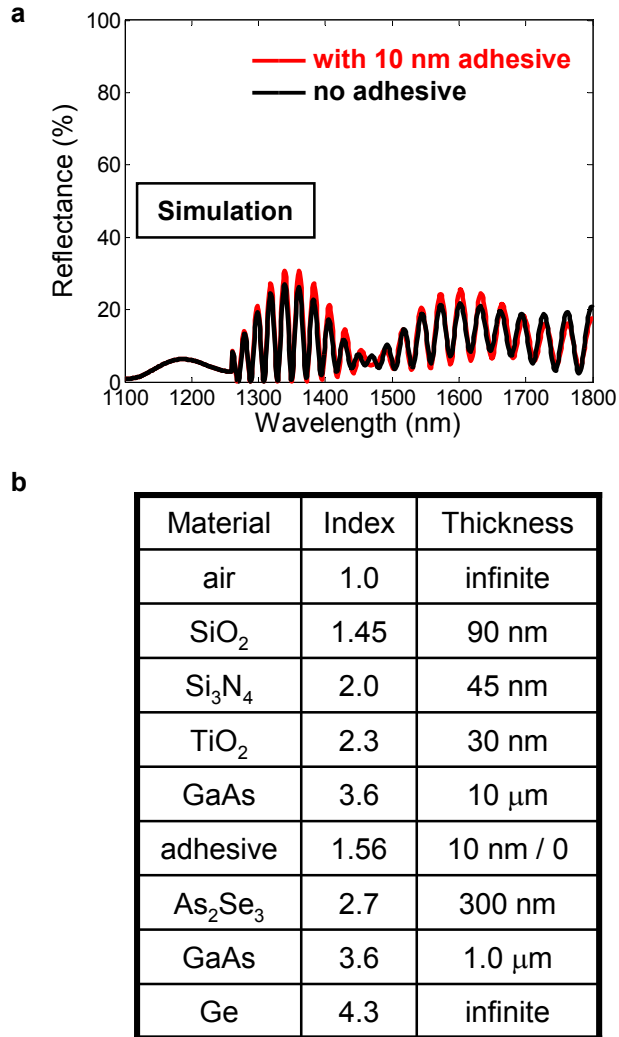
a

b

Material	Index	Thickness
air	1.0	infinite
SiO_2	1.45	90 nm
Si_3N_4	2.0	45 nm
TiO_2	2.3	30 nm
GaAs	3.6	10 μm
adhesive	1.56	10 nm / 0
As_2Se_3	2.7	300 nm
GaAs	3.6	1.0 μm
Ge	4.3	infinite

Figure S21. (a) Simulated reflection spectra for the 3J/Ge cell (using 300 nm As_2Se_3 as interface) with and without 10 nm adhesive layer (InterVia 8023-10), showing similar reflection responses. (b) Layer structure used in the simulation.

a

b

Material	Index	Thickness
air	1.0	infinite
SiO_2	1.45	90 nm
Si_3N_4	2.0	45 nm
TiO_2	2.3	30 nm
GaAs	3.6	10 μm
adhesive	1.56	10 nm
As_2Se_3	2.7	varied
GaAs	3.6	1.0 μm
Ge	4.3	infinite
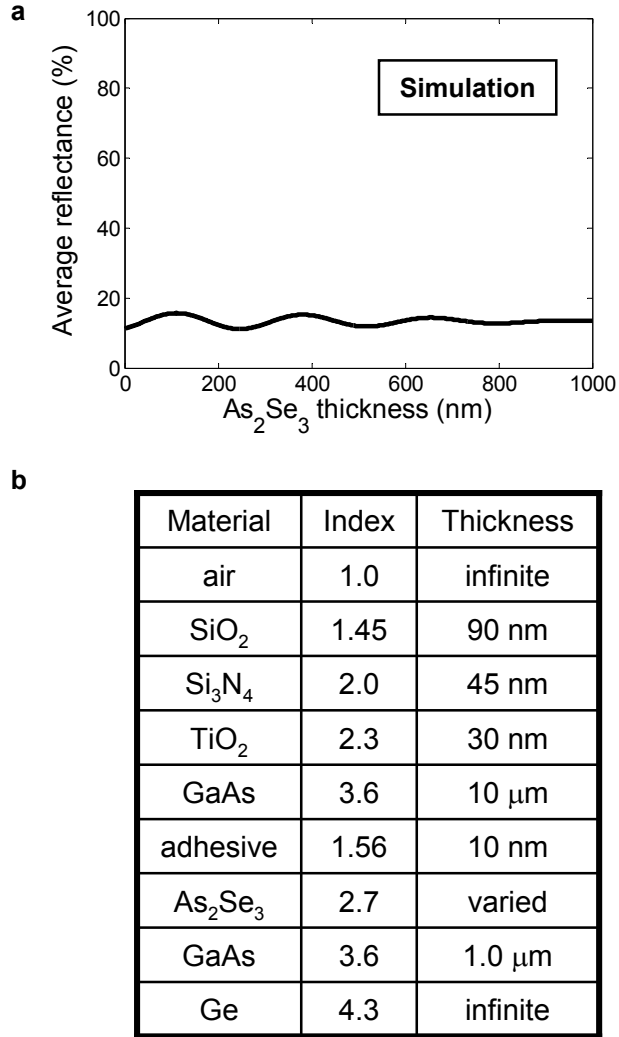
Figure S22. (a) Simulated reflectance (averaged between 1300 nm and 1700 nm) for the stacked 3J/Ge cell as a function of the As_2Se_3 thickness at the interface. The results show that the interface reflection is slightly dependent on the As_2Se_3 thickness. (b) Layer structure used in the simulation.

a

b
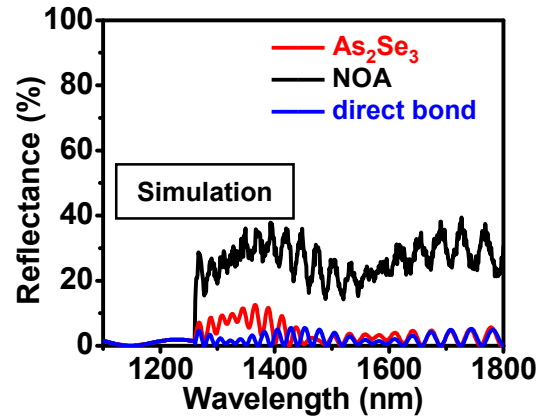
Material		Index	Thickness
perfect ARC (no reflection)		-	-
GaAs		3.6	10 μm
interface	As$_2$Se$_3$	2.7	300 nm
	NOA	1.56	10 μm (incoherent)
	direct bond	-	-
GaAs		3.6	1.0 μm
Ge		4.3	infinite

Figure S23. (a) Simulated reflection spectra for 3J/Ge cells with different interfaces, assuming a perfect ARC is applied between air and the cells. (b) Layer structure used in the simulation.
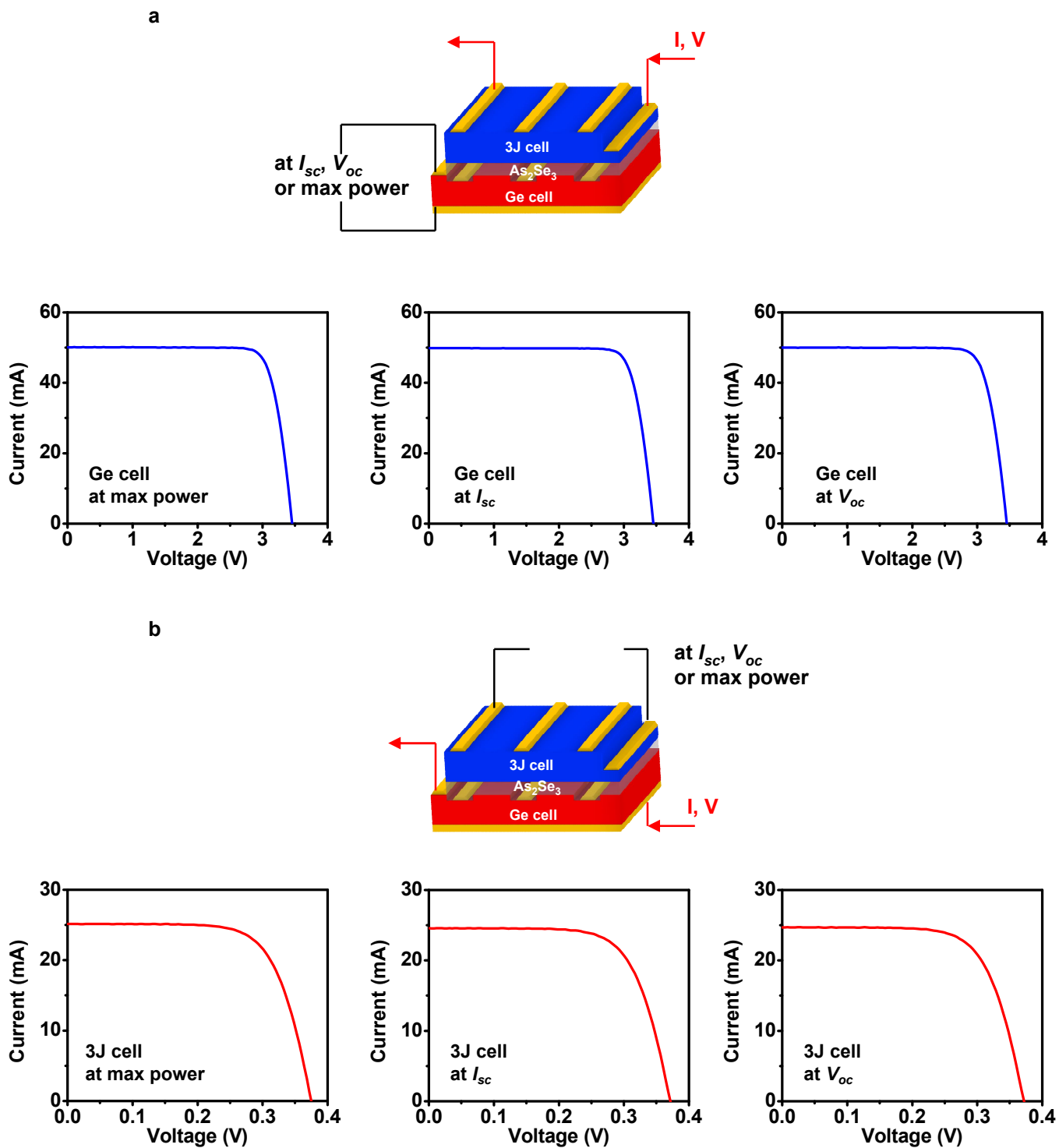
Figure S24. Measured current-voltage curves for each cell under concentrations (~1000 suns), when the other cell is at I_{sc}, V_{oc} or maximum power. The results show that the 3J cell and Ge cell in the stack work independently without optical and electronic coupling.
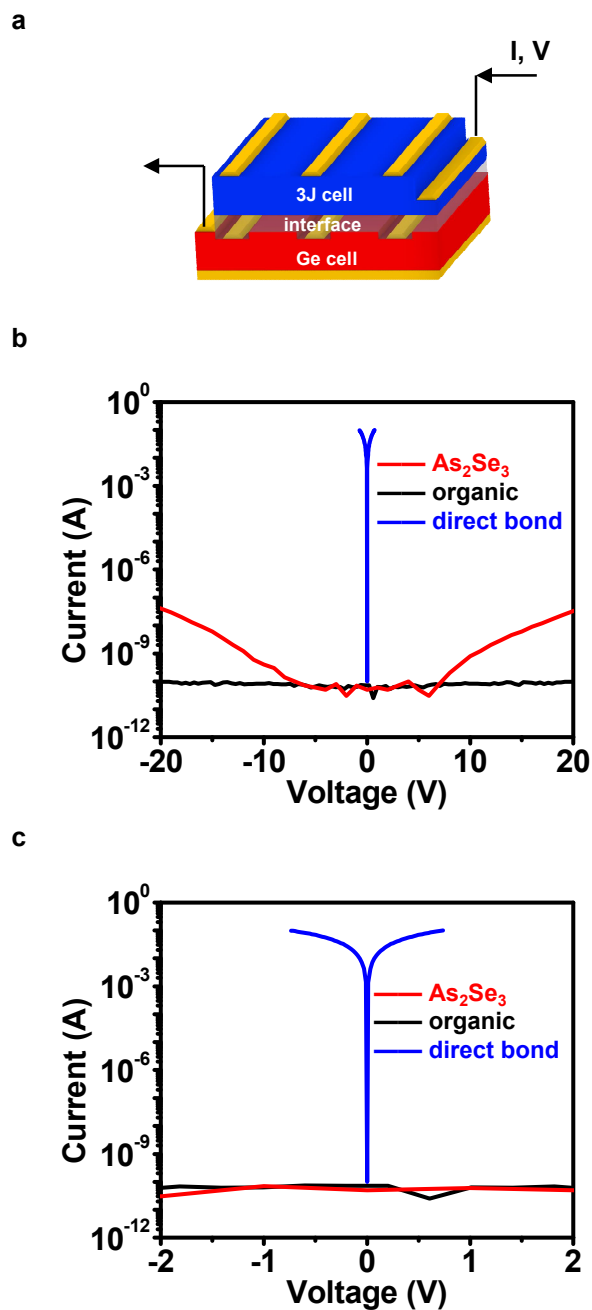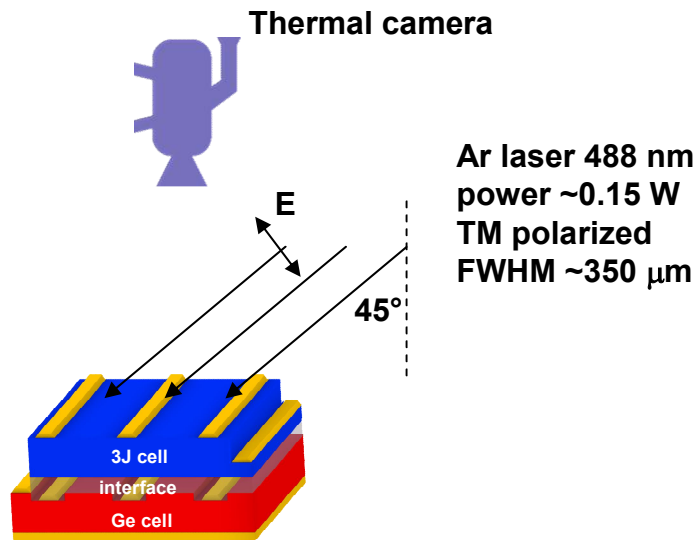
Figure S25. (a) Measurements between the bottom p-contact for the 3J cell and the top n-contact for the Ge cell, for cells with different interfaces (also shown in Fig. 3b). (b) IV curves from - 20 V to + 20 V. (c) IV curves from - 2 V to + 2 V. The detection limits for the current meter are from 10^{-10} A to 10^{-1} A. The resistivities for As_2Se_3 and NOA are measured to be $\sim 10^{10}$ Ω*cm and $\sim 10^{11}$ Ω*cm, respectively.

a

Thermal camera

E

45°

Ar laser 488 nm
power ~0.15 W
TM polarized
FWHM ~350 μm

3J cell
interface
Ge cell

b

Material		thermal conductivity (W/K/m)	Thermal expansion coefficient (10^{-6} K^{-1})	Young's modulus (GPa)	Thickness
air		0.02	-	-	infinite
GaAs		55	6.0	85.5	10 μm
interface	As$_2$Se$_3$	1.0	60	15	300 nm
	NOA	0.17	250	1.0	10 μm
	direct bond	-	-	-	-
Ge		60	6.0	103	230 μm
Steel plate		50	-	-	10 cm
Heat sink (at 25 °C)		infinite	-	infinite	infinite

Figure S26. (a) Experimental setup for temperature measurements under laser heating. (b) Layer structure and material properties used in thermal simulations by Finite Element Analysis (FEA). Experiment and simulation results are shown in Fig. 3f and 3g, respectively. An interfacial thermal conductivity of 85000 W/K/m^2 (very good thermal contact) is prescribed to simulate the contact interface between the Ge substrates and the stainless steel based optical stage.
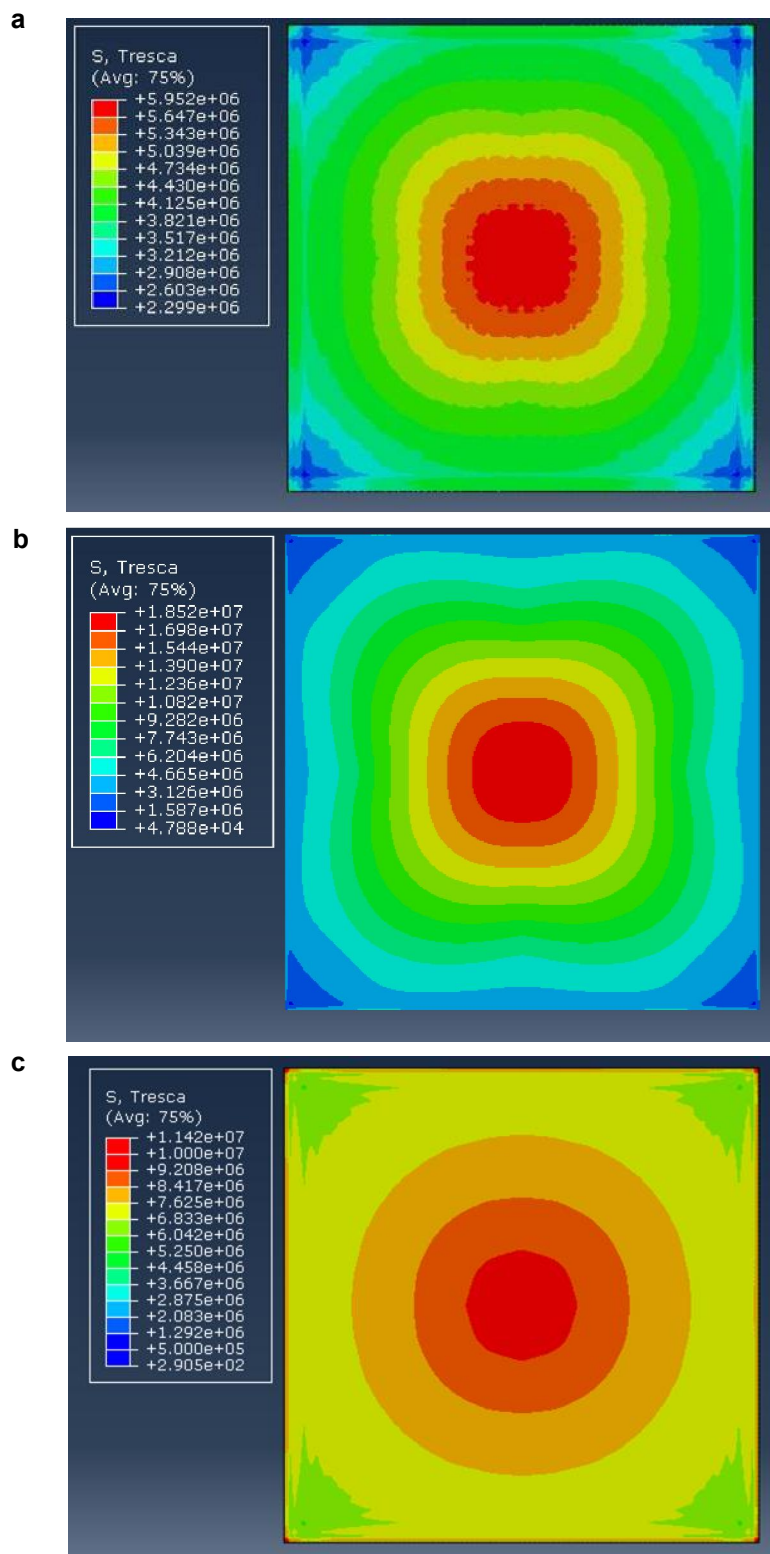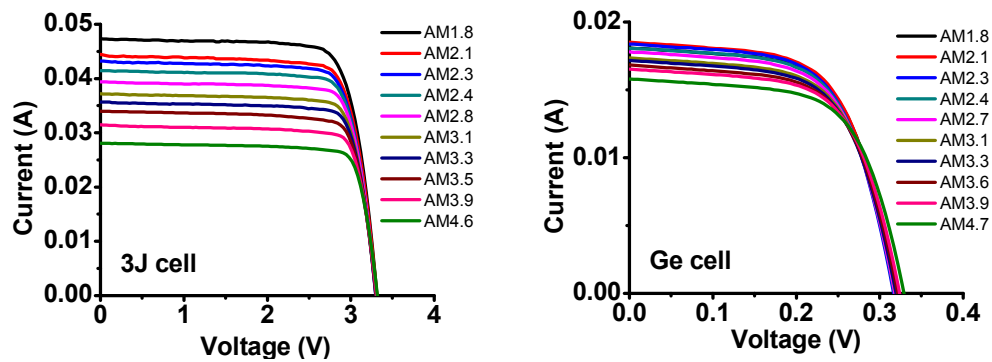
Figure S27. Simulated FEA results for Tresca stresses at the interface between 3J cells and its adjacent interface layers under laser heating, for the cases of (a) 300 nm As$_2$Se$_3$; (b) 10 µm NOA; (c) direct bonding. The unit shown in scale bars is Pa.
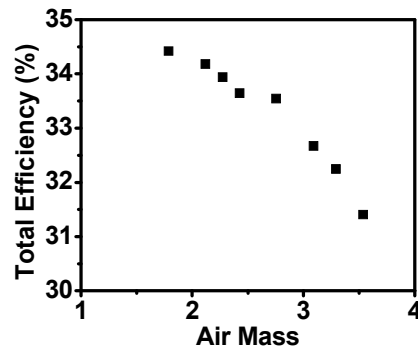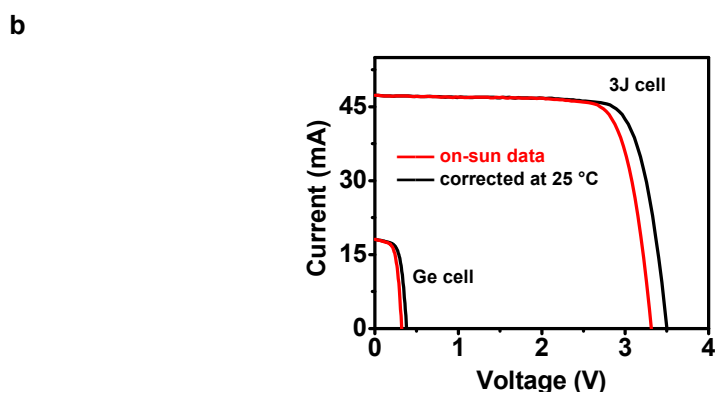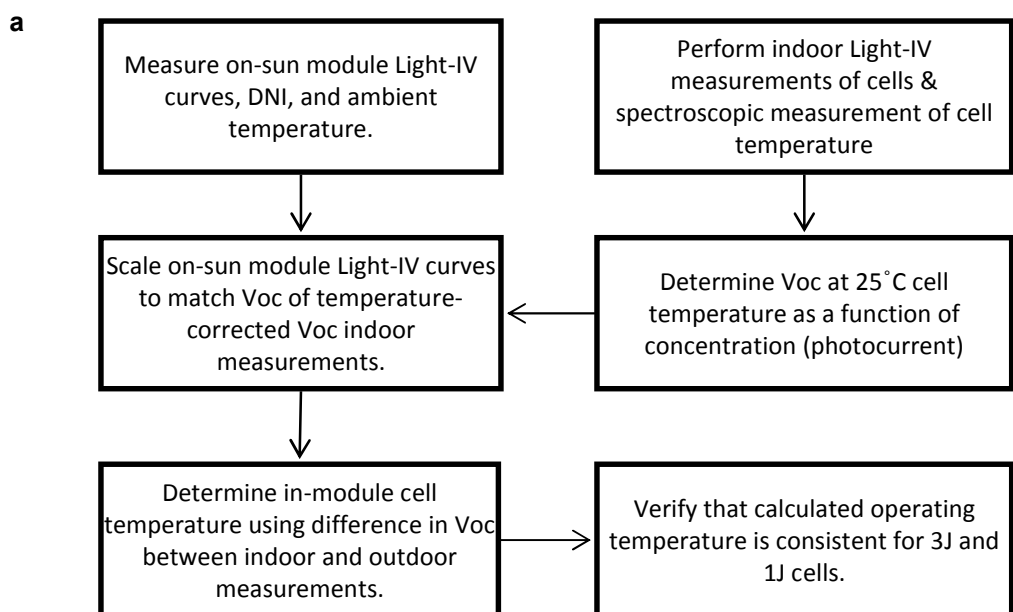
Figure S28. (a) Photograph of an assembled 3J/Ge cell module with concentration optics (Fig. 4a and 4b) installed for testing under the sun. (b) *I–V* curves of the module. A pair of curves, one for the 3J cell and the other for the Ge cell, were collected under a range of air mass conditions corresponding to different times of the day. (c) Total efficiency (3J + Ge) versus air mass as measured on sun by comparison to simultaneously measured direct normal irradiance (DNI): efficiency = P_{max} / (DNI*Aperture area). Measurement time, date and location: 13:00–16:00, Nov. 14, 2013 at Durham, NC, USA.

a

| Measure on-sun module Light-IV curves, DNI, and ambient temperature. | Perform indoor Light-IV measurements of cells & spectroscopic measurement of cell temperature |

Scale on-sun module Light-IV curves to match Voc of temperature-corrected Voc indoor measurements. ← Determine Voc at 25˚C cell temperature as a function of concentration (photocurrent)

Determine in-module cell temperature using difference in Voc between indoor and outdoor measurements. → Verify that calculated operating temperature is consistent for 3J and 1J cells.

b

c

	On-sun V_{oc} (V)	V_{oc} 25˚C (V)	dV_{oc}/dT (V/˚C)	On-sun Cell Temperature (˚C)
3J	3.315	3.501	0.0047	64.5
Ge Cell	0.320	0.380	0.0016	63.2

Figure S29. On-sun module light-*IV* data and adjustment to account for cell heating in-module. (a) method for determining module performance with cell temperature at 25˚C. (b) raw light-*IV* data from on-sun module measurements and adjusted curves obtained through the method of (a). (c) tabulated V_{oc} data from raw on-sun module measurements and indoor measurements. On-sun measurements for this analysis were collected on November 14th in Durham, North Carolina at 1:09 pm. Air Mass at the time of measurement was 1.8, DNI was 914 W/m², and air temperature was 14˚C. For indoor measurements, 4 lasers were selected to excite each sub-cell. Lasers were tuned to match currents in each of the 3 upper sub-cells and to produce roughly half of the current in the Ge cell. dV_{oc}/dT values for the 3J cell were determined using the same laser set-up, varying the temperature of the chuck underneath the cells. dV_{oc}/dT for the Ge cell was estimated at one third of the value of dV_{oc}/dT for the 3J.
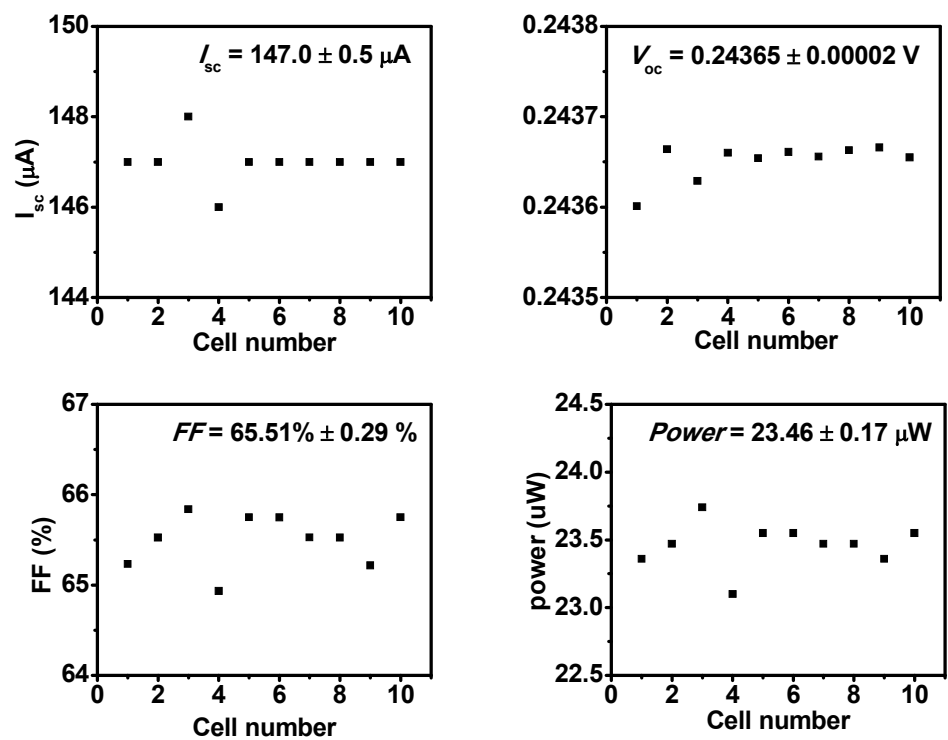
Figure S30. Statistical variations in I_{sc}, V_{oc}, *FF* and power measured for 10 bare Ge cells (no stack, no ARC) under standard AM1.5D one-sun illumination.
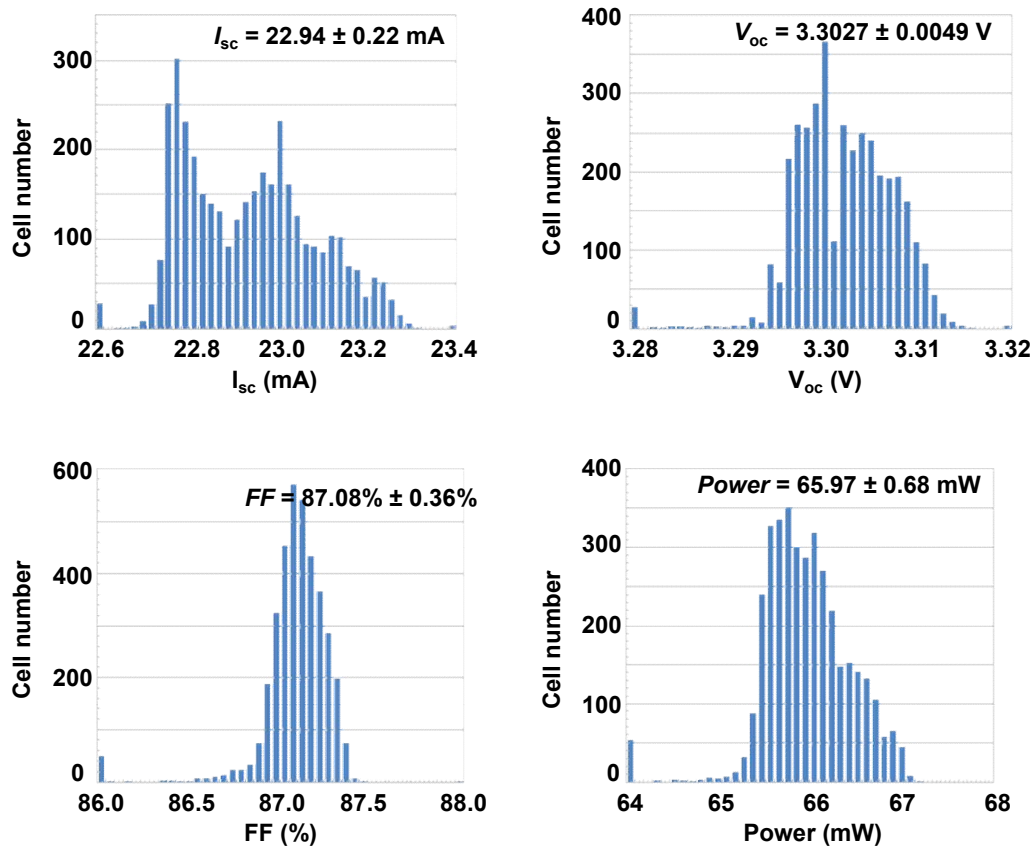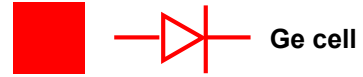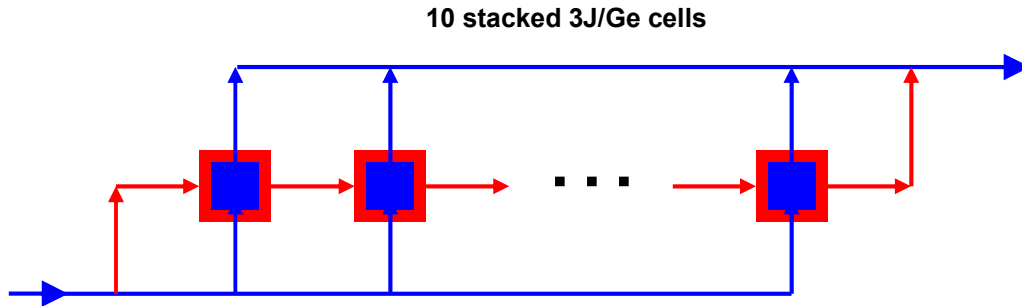
Figure S31. Statistical variations in I_{sc}, V_{oc}, FF and power measured for about 4000 3J cells released on a ceramic substrate, under concentrated illumination (with a power equivalent to ~ 400 suns).
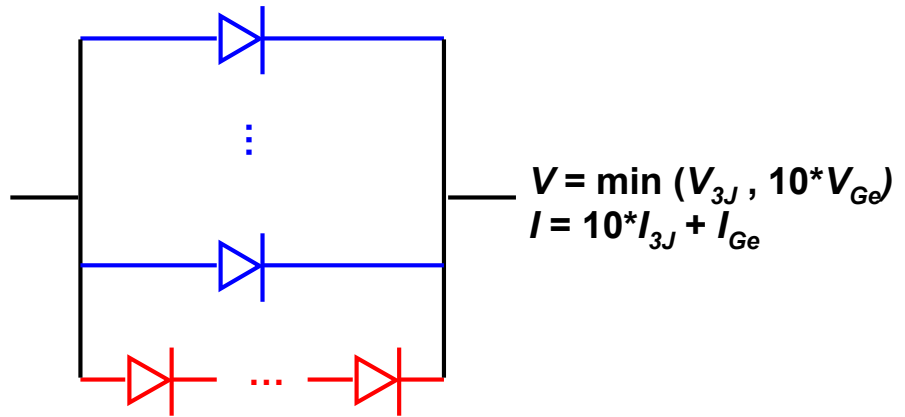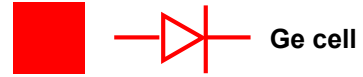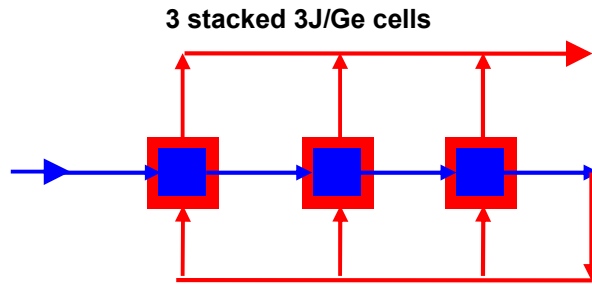
Figure S32. Designed voltage matching interconnected scheme and equivalent circuit diagram for a module array with 10 3J/Ge cells.

3J cell

Ge cell

a. interconnect scheme

3 stacked 3J/Ge cells

b. circuit diagram

$$V = 3*V_{3J} + V_{Ge}$$
$$I = \min (I_{3J}, 3*I_{Ge})$$

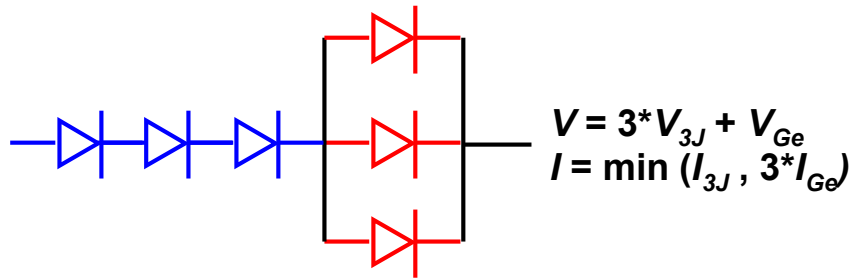**Figure S33.** Designed current matching interconnected scheme and equivalent circuit diagram for a module array with 3 3J/Ge cells.

a

voltage-matching design
10 stacked 3J/Ge cells

$\eta = 35.89\% \pm 0.24\%$

perfect array
(no variation)
$\eta = 36.47\%$

b

current-matching design
3 stacked 3J/Ge cells

$\eta = 36.15\% \pm 0.34\%$

perfect array
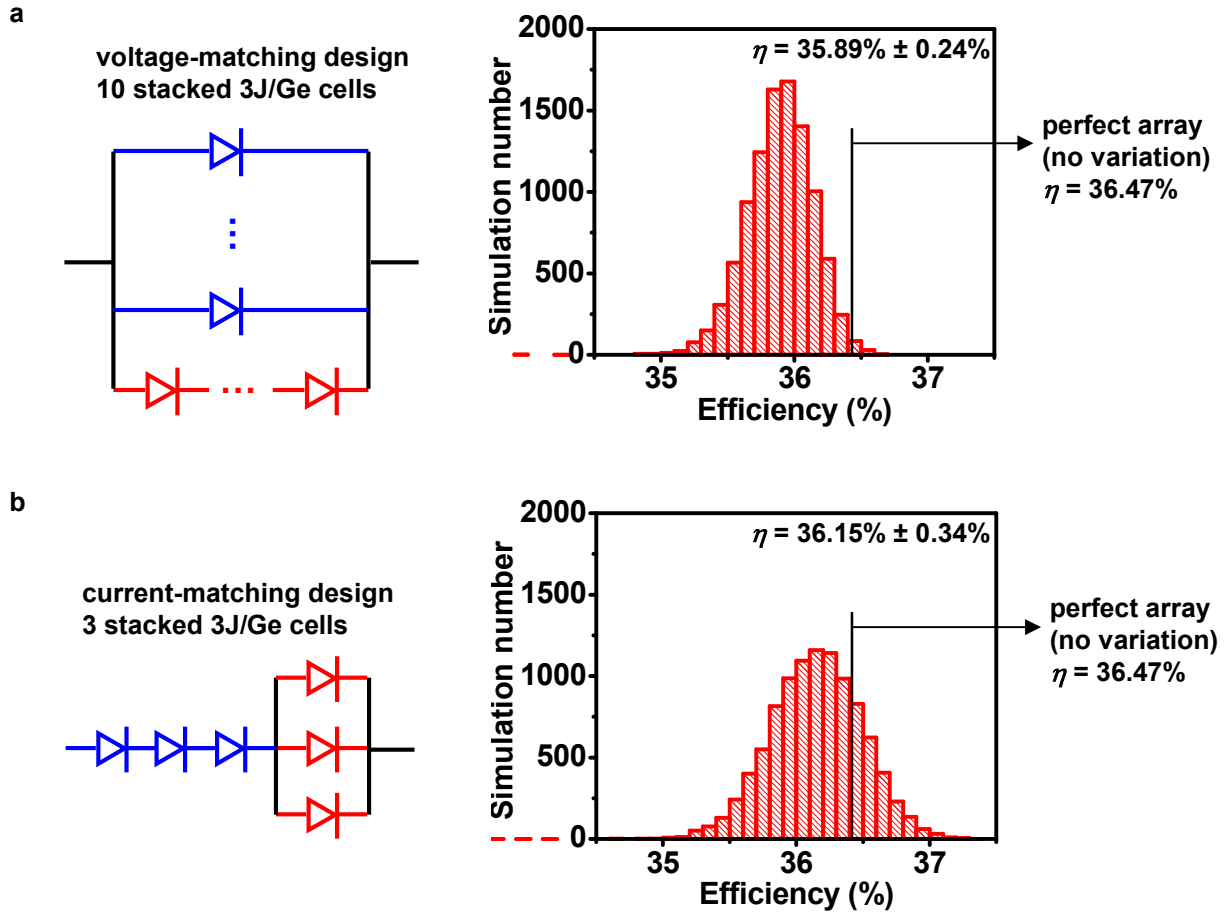(no variation)
$\eta = 36.47\%$

Figure S34. Theoretically predicted module performance including the measured cell variation results (Fig. S30 and S31), assuming both measured current and voltage have a standard deviation of about 1%. (a) Voltage-matching design. (b) Current-matching design.
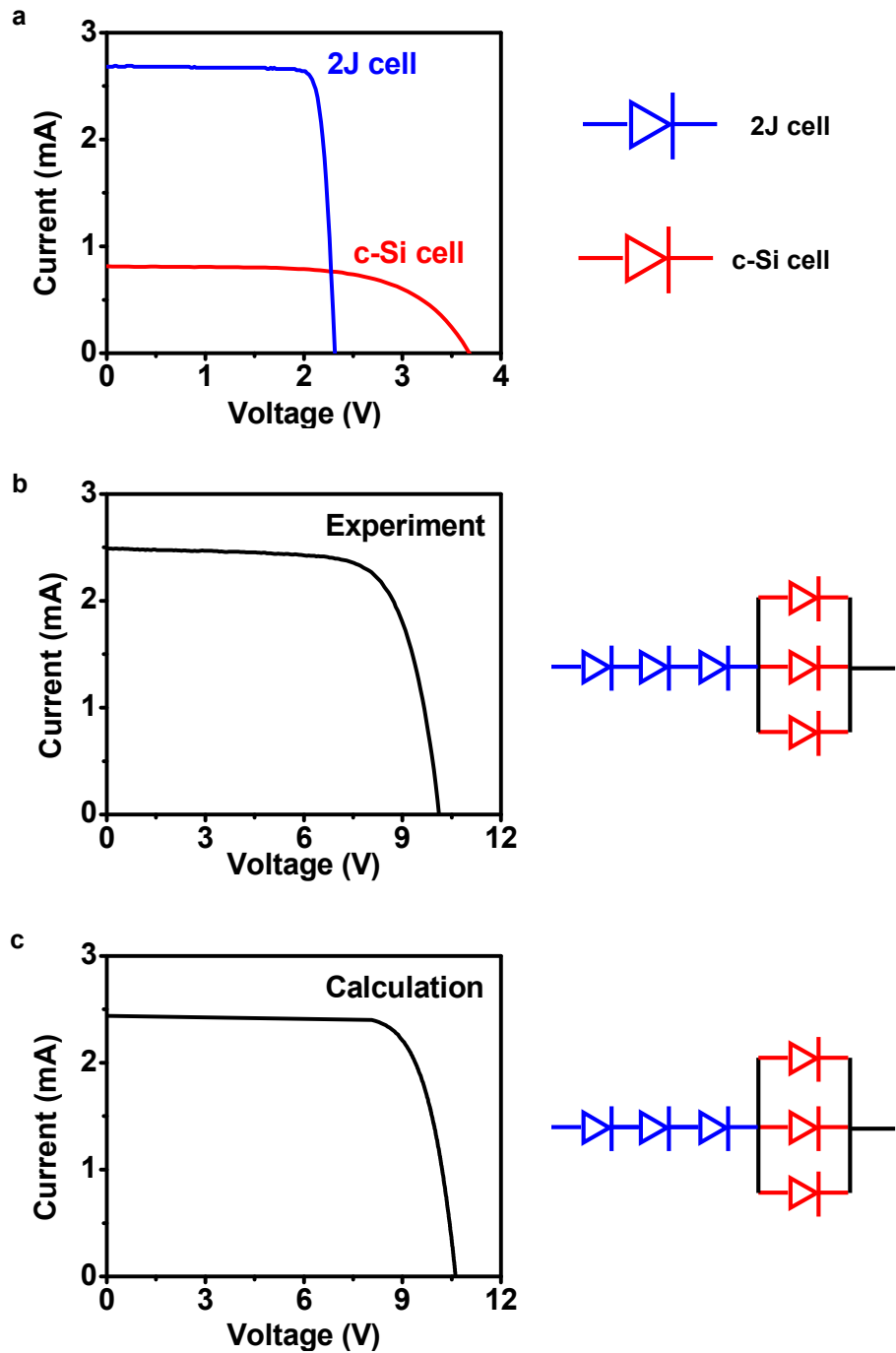
Figure S35. Demonstration of a current matching network using commercial interconnected c-Si (single-crystalline Si) and 2J (double-junction InGaP/GaAs) cells. (a) Measured *I–V* curves for the individual 2J and c-Si cells under one-sun illumination (AM1.5D spectrum). The c-Si cells consist of several Si pn junctions connected in series. (b) Experimental and (c) Calculated *I–V* curves for a current-matching network formed with 3 2J cells and 3 c-Si cells, as illustrated in the circuit schematics.